

PASSIVE TRACERS IN ATHENA: IMPLEMENTATION AND
APPLICATIONS TO TURBULENT STAR FORMATION

ELIZABETH J. PAUL

A SENIOR THESIS
PRESENTED TO THE FACULTY
OF PRINCETON UNIVERSITY
IN CANDIDACY FOR THE DEGREE
OF BACHELOR OF THE ARTS

RECOMMENDED FOR ACCEPTANCE
BY THE DEPARTMENT OF
ASTROPHYSICAL SCIENCES

ADVISER: DR. EVE OSTRIKER

MAY 1, 2015

I hereby declare that I am the sole author of this thesis.

I authorize Princeton University to lend this thesis to other institutions or individuals for the purpose of scholarly research.

Elizabeth J. Paul

I further authorize Princeton University to reproduce this thesis by photocopying or by other means, in total or in part, at the request of other institutions or individuals for the purpose of scholarly research.

Elizabeth J. Paul

Abstract

We implement two passive tracer schemes in the magnetohydrodynamic code ATHENA: a Monte Carlo method by which tracers are moved probabilistically according to the mass flux from a grid cell, and a second-order in time passive tracer scheme which integrates the equation of motion based on the velocity interpolated to a particle's location. Due to its relative computational efficiency, we apply the Monte Carlo method to the numerical simulation of isothermal turbulence in a molecular cloud. We deposit tracers in dense cores above certain threshold densities and follow the subsequent collapse of the GMC. We present results of decaying turbulence of clouds with initial $\alpha_{vir} = 1$ and $\alpha_{vir} = 1.5$. Although the majority of the gas from both high and low density regions eventually collapses, we find that at earlier times, $t \sim t_{ff}$, a much larger proportion of the stellar mass comes from tracers initially in high density regions. This suggests that stars may initially accrete material from the highest-density regions and then accrete from successively lower-density regions. Our results may also imply a relationship between pre-stellar core density and collapse time.

Acknowledgments

I would first and foremost like to thank Eve, for your continued guidance, your helpful feedback throughout the writing process, and for your support through times of discouragement. Thank you for your willingness to take time out of your week to meet with me regularly. Thank you for offering solutions in constructing a model that would work with my time constraints. I would also like to thank Aaron Skinner, for your technical advice with visualization and output and your mentorship throughout the summer on the project that evolved into this work. I would also like to thank my fellow artichokes of the 2 Dickinson Street co-op, who never failed to provide me with good company, strong coffee, and an overabundance of miso soup and coconut milk. Special thanks to Jessica, purveyor of morning breakfast hugs and thesis sustenance.

I would also like to acknowledge the computational resources of the Princeton Institute for Computational Science and Engineering (PICSciE) through the Hecate system. I also acknowledge all the developers of ATHENA and the associated isothermal turbulence model used in this work.

Contents

Abstract	iii
Acknowledgments	iv
1 Introduction	1
1.1 Molecular Clouds - The Birthplace of Stars	1
1.2 Classical Models of Collapse	2
1.2.1 Jeans Instability	2
1.2.2 Virial Mass	5
1.3 Star Formation and Turbulence	6
1.4 Size-Linewidth Relation	8
1.5 Initial Mass Function	9
1.6 Magnetohydrodynamics and ATHENA - A Motivation for Tracers . .	11
2 Methods	14
2.1 ATHENA Code	14
2.2 Passive Tracer Methods	15
2.2.1 Velocity Field Tracers	16
2.2.2 Monte Carlo Tracer Particles	18
2.3 Sink Particles in ATHENA	20
3 Evaluation of Tracer Methods	22
3.1 Advection of a Circle	22

3.2	Blast Wave	29
3.3	Bonnor-Ebert Sphere	34
4	Turbulence Problem	36
4.1	Evaluation of Passive Tracer Method with Turbulence Problem	38
4.1.1	$n_{tracer} = 1$	38
4.1.2	$n_{tracer} = 5$	41
5	Turbulent Star Formation with Tracers - Results	47
5.1	Parameterization	47
5.2	$\alpha_{vir} = 1$, Tracers deposited at $t = 4.9$ Myr	48
5.2.1	Initial Tracer Distribution	50
5.2.2	Final Tracer Distribution	53
5.2.3	Discussion and Analysis	56
5.3	$\alpha_{vir} = 1$, Tracers deposited at $t = 0.98$ Myr	57
5.3.1	Initial Tracer Distribution	58
5.3.2	Final Tracer Distribution	61
5.3.3	Analysis and Discussion	64
5.4	$\alpha_{vir} = 1.5$, Tracers deposited at $t = 4.9$ Myr	67
5.4.1	Initial Tracer Distribution	68
5.4.2	Final Tracer Distribution	72
5.4.3	Analysis and Discussion	76
6	Conclusions and Future Work	78
6.1	Summary of Results and Conclusions	78
6.2	Future Work	80

Chapter 1

Introduction

1.1 Molecular Clouds - The Birthplace of Stars

All star formation takes place in molecular clouds, dense regions within the interstellar medium in which the gas is mostly molecular hydrogen (H_2) with some He. Molecular clouds are traditionally detected from the $J = 1 \rightarrow 0$ transition of CO (Draine (2010)), as H_2 is difficult to detect from radio or infrared emission. A spatially resolved map of this tracer molecule can be related to the H_2 surface density by a conversion factor, $X_{\text{CO}} = 1.8 \times 10^{20} \text{ H}_2 \text{ cm}^{-2} / \text{K km s}^{-1}$ (Dame et al. (2001)), although the actual value depends on the cloud parameters.

While almost all giant molecular clouds (GMCs) show evidence of star formation, some smaller molecular clouds may not be star-forming (Blitz (1993)). Typical GMCs have masses $\sim 1 - 2 \times 10^5 M_\odot$, diameters of $\sim 45 \text{ pc}$, $\langle n_{\text{H}_2} \rangle \sim 50 - 10^2 \text{ cm}^{-3}$, and show well-defined boundaries (Blitz (1993)). Observationally-supported models put typical GMC lifetimes at $\sim 30 \text{ Myr}$ (Bash et al. (1977)). GMCs are observed to have temperatures $\sim 8 - 10 \text{ K}$ (Dobbs et al. (2014)).

GMCs are inhomogeneous structures, containing dense clumps and filaments at a wide range of scales (Blitz (1993)). The internal structure of GMCs can be at-

tributed to gravitational collapse, supersonic turbulence, and colliding flows (Dobbs et al. (2014)). Clumps are the massive regions out of which star clusters are born. Within clumps and filaments are cores, the over-dense regions that eventually undergo gravitational collapse to form an individual star or a stellar system (Williams et al. (2000)).

Material within GMCs have random turbulent motions generally exhibiting highly supersonic velocities (Larson et al. (1980)). Since the turbulent velocities would decay on timescales comparable to $\tau = L/v_{turb}$, the turbulent velocities would not be maintained for long periods of time without a source of driven turbulence. Proposed sources for non-thermal motions include global collapse and hierarchical fragmentation (Vázquez-Semadeni et al. (2009)), external driving sources such as accretion flows and galactic scale motions (Dobbs et al. (2012)), and internal driving sources such as radiation pressure and outflows (Dekel & Krumholz (2013)).

1.2 Classical Models of Collapse

Star formation takes place as cores within dense molecular clouds become gravitationally unstable and runaway collapse occurs. We consider several simple physical models for the development of gravitational instability and their associated criteria for collapse to occur.

1.2.1 Jeans Instability

We begin with a simplified physical model for gravitational collapse: a non-rotating, uniform density, unmagnetized cloud (Jeans (1928)). We look at the conditions under which an initial equilibrium state $(\rho_0, P_0, v_0, \Phi_0)$ becomes unstable to small perturbations $(\rho_1, P_1, v_1, \Phi_1)$. We begin with the hydrodynamic equations of mass and

momentum conservation,

$$\frac{\partial \rho}{\partial t} + \nabla \cdot (\rho \mathbf{v}) = 0 \quad (1.1)$$

$$\frac{\partial \mathbf{v}}{\partial t} + (\mathbf{v} \cdot \nabla) \mathbf{v} = -\frac{1}{\rho} \nabla P - \nabla \Phi \quad (1.2)$$

along with Poisson's equation,

$$\nabla^2 \Phi = 4\pi G \rho. \quad (1.3)$$

We can apply the ideal fluid approximation to describe molecular clouds, as viscosity is negligible at the scales of interest for self-gravity in the interstellar medium (Ward-Thompson & Whitworth (2011)). We use an isothermal equation of state $P = \rho c_s^2$, as temperatures are observed to vary only weakly within GMCs. We have that the state at a given time, (ρ, P, v, Φ) , is a combination of the equilibrium solution with perturbations:

$$\rho = \rho_0 + \rho_1 \quad (1.4)$$

$$P = c_s^2(\rho_0 + \rho_1) \quad (1.5)$$

$$v = v_1 \quad (1.6)$$

$$\Phi = \Phi_0 + \Phi_1. \quad (1.7)$$

Plugging 1.4, 1.5, 1.6, and 1.7 into 1.1 and 1.2, and using 1.3, we can ignore second order terms of ρ_1 and v_1 to arrive at

$$\frac{\partial \rho_1}{\partial t} + \rho_0 \nabla \cdot \mathbf{v}_1 = 0 \quad (1.8)$$

$$\rho_0 \frac{\partial \mathbf{v}_1}{\partial t} = -c_s^2 \nabla \rho_1 - \nabla \Phi_1 \quad (1.9)$$

$$\nabla^2 \Phi_1 = 4\pi G \rho_1. \quad (1.10)$$

This linear system of differential equations has plane wave solutions for ρ_1 , v_1 , and Φ_1 of the form $\exp[i(\mathbf{k} \cdot \mathbf{x} + \omega t)]$. We have the associated dispersion relation,

$$\omega^2 = k^2 c_s^2 - 4\pi G \rho_0. \quad (1.11)$$

If $k < k_J$ where

$$k_J = \left(\frac{4\pi G \rho_0}{c_s^2} \right)^{1/2}, \quad (1.12)$$

ω will be imaginary and the perturbations will grow. We can use this critical wavenumber to define the Jeans length, $\lambda_J = \frac{2\pi}{k_J}$, the minimal scale at which the cloud becomes gravitationally unstable. We can define the Jeans Mass as the mass contained within a sphere of diameter λ_J ,

$$M_J = \frac{4\pi}{3} \rho_0 \left(\frac{\lambda_J}{2} \right)^3 = \frac{\pi^{5/2}}{6} \frac{c_s^3}{G^{3/2} \rho_0^{1/2}}. \quad (1.13)$$

While simple, the Jeans picture is not physically realistic as it makes the assumption that $\nabla^2 \Phi_0 = 0$ rather than $4\pi G \rho_0$, yet we assume Poisson's equation to hold for perturbations, $\nabla^2 \Phi_1 = 4\pi G \rho_1$. Furthermore, because almost all observed molecular clouds exhibit clumping and dense filaments, the uniform density background criterion is not realistic. In fact, almost all large molecular clouds have supersonic turbulent velocities which generate inhomogeneities in an initially uniform density cloud (Larson (1981)).

Although the Jeans analysis is flawed, the Jeans instability serves as an approximate criterion for collapse during star formation (Draine 2010). In fact, up to a constant factor, the Jeans mass is similar to the maximum mass for an isothermal sphere confined by external pressure, $P_e = \rho_e c_s^2$. Bonnor and Ebert (Ebert (1955),

Bonnor (1956)) show that this maximum mass is given by,

$$M_{BE}(P_e) = \frac{1.18 c_s^4}{(G^3 P_e)^{1/2}} = 0.4 M_J. \quad (1.14)$$

According to the classical Jeans instability, all observed molecular clouds with $M \geq 100 M_\odot$, $R \geq 1$ pc, and $T < 30$ K would be unstable to gravitational collapse assuming constant density. However, observations show evidence that low mass dense cores ($\sim M_\odot$) can collapse into stars within clouds that are not undergoing global collapse (Bonazzola et al. (1987)). This evidence shows that the classical Jeans picture is too simple, as it assumes that fragmentation allows small-scale collapse after the GMC becomes unstable on large scales. We need a theory that accounts for supersonic turbulence rather than assuming that thermal energy provides the dominant support in molecular clouds.

1.2.2 Virial Mass

We can make a more general statement about mass stability using the virial theorem. For an unmagnetized, non-rotating region in equilibrium we have that,

$$E_{grav} + 2K = 0 \quad (1.15)$$

where E_{grav} is the total gravitational potential energy and K is the total kinetic energy. For a total 3-dimensional velocity dispersion σ (including thermal and non-thermal components), we have that

$$K = \frac{1}{2} M \sigma^2 \quad (1.16)$$

and

$$E_{grav} = -\frac{3}{5} \alpha \frac{GM^2}{R} \quad (1.17)$$

where $\alpha = 1$ for a uniform mass distribution. This gives us a virial mass,

$$M_{vir} = \frac{5\sigma^2 R}{3\alpha G} \sim \frac{5\sigma^2 R}{3G}. \quad (1.18)$$

If the mass of a cloud is similar to M_{vir} , it will be in virial equilibrium, but it will collapse if $M_{GMC} \gg M_{vir}$. Since M_{vir} scales with σ^2 , a higher non-thermal turbulent velocity dispersion may support a molecular cloud against collapse (Ward-Thompson & Whitworth (2011)).

The virial parameter,

$$\alpha_{vir} = \frac{M_{virial}}{M_{GMC}} = \frac{5\sigma^2 R}{3GM_{GMC}}, \quad (1.19)$$

is defined such that $\alpha_{vir} = 1$ for a uniform unmagnetized sphere in virial equilibrium. The typical value of α_{vir} from observations of GMCs is ~ 1 , although it can range from ~ 0.1 to ~ 10 (Dobbs et al. (2014)).

The timescale that defines the dynamics of self-gravitating clouds is the free-fall time, the time needed for a spherical cloud to collapse to a point due to gravity ignoring pressure forces:

$$t_{ff} = \left(\frac{3\pi}{32G\rho} \right)^{1/2}. \quad (1.20)$$

1.3 Star Formation and Turbulence

Molecular clouds observationally are not consistent with the simplified classical picture of gravitational collapse. As discussed in §1.1, most often they feature inhomogeneous clumping and supersonic turbulent motions. Turbulence can be defined as the cascade of large-scale systematic motions to small-scale chaotic motion. Turbulent motion is characterized by the relationship between a turbulent velocity, v_{turb} , or velocity dispersion, σ_v , for a given wavenumber k (Larson (1981)). The power spec-

trum, $P(\mathbf{k}) = |\mathbf{v}(\mathbf{k})|^2$, describes the distribution of turbulent velocities for a given wavenumber k , which can directly related to a length scale, $l = \frac{2\pi}{k}$, assuming isotropy of motion within the cloud. Turbulence in molecular clouds typically decays within a crossing time, $t_{cross} = L/v_{turb}$, where L is the length scale of the GMC (Stone et al. (1998)).

According to classical Kolmogorov theory, the energy cascades down from $k_{min} = \frac{2\pi}{L}$, where L is the largest length scale, to the minimum length scale, the Reynolds scale. The assumption is that energy is transferred from larger to smaller scales until it is eventually dissipated by viscosity on the smallest scales (McKee & Ostriker (2007)). If we assume a power law form for the power spectrum, $P(\mathbf{k}) \propto k^{-n}$, it can be shown that

$$v(L) \sim \sigma(L) \sim L^{(n-3)/2}. \quad (1.21)$$

Specifically for Komogorov turbulence with $n = 11/3$,

$$v(L) = v(L_0)(L/L_0)^{1/3}, \quad (1.22)$$

where L_0 is the Reynolds scale.

Classical Kolmogorov turbulence theory assumes subsonic velocities ($v < c_s$) in incompressible flows. However, observations show that in general velocities in molecular clouds are large compared to c_s at scales above individual pre-stellar cores, so we cannot expect Kolmogorov theory to apply exactly. Energy is often transferred from large to small scales through large-scale hydrodynamic or MHD shocks, generated by supernovae or other bulk motions (McKee & Ostriker (2007)).

Burgers turbulence considers the power spectrum for a system of overlapping shocks in a fluid without pressure (Frisch & Bec (2001)). It is characterized by a power spectrum,

$$P(\mathbf{k}) \propto k^{-4} \propto L^4 \quad (1.23)$$

This spectrum gives a scaling relation,

$$v(L) \propto L^{1/2}. \quad (1.24)$$

Recent high-resolution supersonic ($\mathcal{M} = 17$) hydrodynamic simulations have shown support for this velocity scaling relation for both solenoidal ($\nabla \cdot \mathbf{v} = 0$) and compressive ($\nabla \times \mathbf{v} = 0$) driving modes (Federrath (2013)).

1.4 Size-Linewidth Relation

Observations of interstellar motions provide evidence for turbulent scaling relations. From observations of several molecular tracers (CO, H₂CO, NH₂, and OH), Larson arrived at a scaling for structures of projected length scale $0.1 \text{ pc} \leq L \leq 10^2 \text{ pc}$ (Larson (1979)),

$$\sigma_v(L) \simeq 1.10 L^{0.38} \text{ km s}^{-1}. \quad (1.25)$$

From more recent higher-resolution observations of GMCs in the Galactic Plane, Heyer et al. derived a scaling relation between L , σ_v , and column density Σ_{GMC} for virial equilibrium (Heyer et al. (2009)),

$$\sigma_v = (\pi G/5)^{1/2} \Sigma_{\text{GMC}}^{1/2} L^{1/2}. \quad (1.26)$$

This relation would imply that the typical velocity scales such that the non-thermal pressure from σ_v balances the self gravity of the cloud. Heyer et al. find that the Galactic Ring Survey clouds follow a similar relation between $\sigma_v/L^{1/2}$ and $\Sigma_{\text{GMC}}^{1/2}$, with a slightly larger coefficient. This relation has also been confirmed from observations of extragalactic GMCs (Wong et al. (2011)).

Applying principal component analysis to spectral maps of GMCs, Roman-Duval

et al. derived a power law scaling relationship,

$$\sigma_v \propto L^\alpha, \quad (1.27)$$

with exponent $\alpha \sim 0.62$ (Roman-Duval et al. (2011)). These steeper scaling relations are more consistent with supersonic conditions associated with Bergers turbulence.

1.5 Initial Mass Function

The Initial Mass Function (IMF) describes the distribution of stellar masses of newly formed stars, defined as,

$$\xi(M) = \frac{dN}{d \log(M)} = k_1 M^{-\Gamma}. \quad (1.28)$$

It was first empirically defined by Salpeter, using the observed luminosity function for the stellar population in the solar neighborhood. He arrived at a simple power law relation (Salpeter (1955)),

$$\xi(M) \approx 0.03(M/M_\odot)^{-1.35}. \quad (1.29)$$

More recent observations of star-count data in the solar neighborhood have inferred an IMF consisting of a 3-part power law (Kroupa (2001)):

$$\frac{dN}{d \log(M)} \propto M^{-1.3}, \quad 0.5 < M/M_\odot < 50 \quad (1.30)$$

$$\frac{dN}{d \log(M)} \propto M^{-0.3}, \quad 0.08 < M/M_\odot < 0.5 \quad (1.31)$$

$$\frac{dN}{d \log(M)} \propto M^{0.7}, \quad 0.01 < M/M_\odot < 0.08. \quad (1.32)$$

Note the similarity in the Salpeter power-law index for the high-mass range. Furthermore, the lack of very high mass ($\sim 1000 M_{\odot}$) stars in all star-forming regions of our galaxy leads to the prediction of a sharp turn-down of the IMF above $\sim 100 M_{\odot}$. This could be due to a decline in star-formation after a turbulent crossing time (Elmegreen (2000)).

One of the objectives of star formation theory is to understand why very little variation in the IMF has been observed between star-forming regions in our galaxy: there do not appear to be measurable deviations from the average IMF between low density molecular clouds and giant molecular clouds or between exotic galaxies and globular clusters (Kroupa (2002)). It appears that the properties of the IMF are independent of density, turbulence, and magnetic field within a cloud (McKee & Ostriker (2007)).

Furthermore, the mass distribution of pre-stellar cores, or the core mass function (CMF), has many similarities to the empirical IMF. It has been fit to a similar power law form with a offset of ~ 2 in their mass ranges (Hennebelle & Chabrier (2008)). This implies that the IMF is determined by the distribution of pre-stellar cores, with the offset most likely due to the star forming efficiency of the cores (Ward-Thompson & Whitworth (2011)).

Given the apparent uniformity of the CMF and IMF, many attempts have been made to derive a theoretical understanding for stellar mass distributions. However, understanding the star formation process is much more complicated than the idealized analytic models for collapse as described in §1.2. Although the similarity between the IMF and CMF may suggest that the IMF is derived from the CMF, this hinges on the assumption that all observed cores are bound to form stars and that all stars must have the same star formation efficiency. Of course this simple picture is not realistic, as cores undergo internal turbulent fragmentation and some cores may disperse without forming stars (Offner et al. (2014)).

It has been suggested that if the thermal pressure within a core, $\rho_c c_s^2$, exceeds the mean turbulent pressure in a cloud, $\langle \rho \rangle \sigma_v^2$, the core will be unstable to collapse (Krumholz & McKee (2005)). Once a core becomes unstable, it typically will collapse within several local free-fall times (Vázquez-Semadeni et al. (2005)),

$$t_{fc} = \frac{L_{J,c}}{c_s} = \left(\frac{\pi}{G\rho_c} \right)^{1/2}, \quad (1.33)$$

where ρ_c is the clump density. However, there have not previously been simulations to test the presence of a threshold density for collapse or the mean collapse time as a function of core properties and the turbulent environment.

Using numerical methods, some have found excellent agreement between calculated and observed mass spectrum. Using high resolution smooth particle hydrodynamic hydrodynamic (SPH) simulations of molecular clouds, Klessen et al. found that interactions between individual cores within a clump can influence the accretion and determine the stellar mass (Klessen et al. (1998)). Hennebelle et al. derived an analytical theory for the CMF based on the thermal or turbulent Jeans mass in addition to selection criteria for clumps produced by supersonic turbulence, predicting a power-law tail and an exponential cut off above the Jeans mass (Hennebelle & Chabrier (2008)). Although many theories have been developed for the IMF, none have yet received widespread support. Detailed tests using numerical simulations are helpful for evaluating proposed hypotheses.

1.6 Magnetohydrodynamics and ATHENA - A Motivation for Tracers

ATHENA is a grid-based code that solves the equations of ideal, compressible magnetohydrodynamics. It was developed for astrophysical applications, such as star

formation and accretion. Designed for its advantages in capturing shocks and discontinuities in astrophysical flows, ATHENA discretizes the MHD equations using volume averages of conserved quantities (Stone et al. (2008)). Grid-based codes use Eulerian schemes to conserve quantities within a given cell. However, as the fluid is mixed on the grid resolution scale, the information about the past evolution of a particular parcel of fluid is lost.

Alternatively, in a smoothed particle hydrodynamic (SPH) scheme the fluid is replaced by a large number of particles. Rather than expressing the conservative equations of hydrodynamics through grid-based quantities, the properties of a particle are smoothed by a kernel function and the local properties are determined from interpolation. Particles are integrated using derived fields (Monaghan (1992)). The use of SPH methods allows one to track the evolution of the properties of a parcel of fluid forward in time. However, SPH methods have been shown to have significant shortcomings because they do not directly integrate the equations of hydrodynamics. SPH has been shown to perform poorly in the modeling of instabilities and has difficulty with shock-capturing (Agertz et al. (2007)). In a detailed comparison between the SPH code, GADGET, and MHD code, AREPO, it has been found that high Mach number shocks were much broader in the SPH case and significant post-shock oscillations developed, while AREPO was able to much better resolve weak shocks (Sijacki et al. (2012)).

However, it is possible to trace the Lagrangian evolution of the fluid in an Eulerian scheme by implementing a tracer particle algorithm. Tracer particles are passively advected with the fluid flow, allowing one to record the movement of a parcel of gas through phase space and record the underlying fluid properties through time. Applied to the study of collapse during turbulent star formation, we can use passive tracer particles in order to probe the initial mass function of a dense core and follow the evolution of turbulently-compressed filaments as they evolve in time.

Passive tracer particles can be applied to many other astrophysical contexts. For example, they have been applied to follow the evolution of gas flows as it settles onto galaxies, allowing them to trace the angular momentum and temperature of galactic gas (Pichon et al. (2011)). They have also been used to trace turbulent mixing of H_2 in self-gravitating molecular clouds, finding mixing timescales on the order of 0.3 Myr (Federrath et al. (2008)). Furthermore, passive tracer particles have been used to not only follow the local properties of a simulation but also to model the microphysics of hydrodynamic simulations. Enßlin and Brüggen used tracers to produce synthetic polarization radio maps of cluster radio relics and to evolve the electron spectrum forward in time (Enßlin & Brüggen (2002)). Passive tracers have been verified to follow the streamlines in simulated Type 1a supernovae and have been used for post-processing nucleosynthesis reaction networks (Brown et al. (2005)). It is clear that passive tracer particles can have many astrophysical applications, and our implementation in ATHENA can easily be adapted according to the user’s needs. Tracers can record additional properties of the fluid, can be spatially distributed according to the fluid properties or according to a specific application, and the implementation could be expanded to model sub-grid physics.

Chapter 2

Methods

2.1 ATHENA Code

ATHENA was developed for the study of astrophysical fluid dynamics, using numerical methods to solve the equations of compressible magnetohydrodynamics. Using higher-order Godunov methods, ATHENA has been demonstrated to have superior capabilities in capturing shocks, such as those that arise during astrophysical turbulent flows. ATHENA solves the equations of ideal MHD in conservative form (Stone et al. (2008)). Here we incorporate ATHENA's self-gravity algorithm. The full set of equations is:

$$\frac{\partial \rho}{\partial t} + \nabla \cdot (\rho \mathbf{v}) = 0, \quad (2.1)$$

$$\frac{\partial(\rho \mathbf{v})}{\partial t} + \nabla \cdot (\rho \mathbf{v} \mathbf{v} - \mathbf{B} \mathbf{B} + \mathbf{P}^*) = -\nabla(\Phi + \Phi_{ext}), \quad (2.2)$$

$$\frac{\partial E}{\partial t} + \nabla \cdot [(E + P^*) \mathbf{v} - \mathbf{B}(\mathbf{B} \cdot \mathbf{v})] = -\rho \mathbf{v} \cdot \nabla(\Phi + \Phi_{ext}), \quad (2.3)$$

$$\frac{\partial \mathbf{B}}{\partial t} - \nabla \times (\mathbf{v} \times \mathbf{B}) = 0, \quad (2.4)$$

$$\nabla^2 \Phi = 4\pi G \rho. \quad (2.5)$$

Here Φ is the gravitational potential, P is the gas pressure, $P^* = P + \frac{B^2}{2}$, and E is the total energy density,

$$E = \frac{P}{\gamma - 1} + \frac{1}{2}\rho v^2 + \frac{B^2}{2}. \quad (2.6)$$

In the turbulence simulations described below, we omit Equations 2.3 and 2.4 because we consider for simplicity an unmagnetized medium with an isothermal equation of state,

$$P = c_s^2 \rho \quad (2.7)$$

where c_s is the isothermal sound speed. In the following simulations we use the van Leer integration scheme, a dimensionally unsplit integrator of the MHD equation which uses a predictor-corrector algorithm. Although it is somewhat more diffusive than other methods, such as the corner transport upwind (CTU) algorithm, it has been shown to perform well in certain regimes, such as supersonic turbulence, and it easily allows for the incorporation of more complex physics, such as self-gravity (Stone & Gardiner (2009)).

2.2 Passive Tracer Methods

We implement two passive tracer schemes in ATHENA, using the van Leer integrator. These particles are advected with the underlying fluid and are used to trace individual parcels of fluid throughout the evolution of the simulation. Tracers can be initialized such that the tracer density is proportional to the underlying fluid density, such that they are uniformly distributed, or they can be placed at a specific time step according to the need in the application. Each tracer particle can store properties such as its initial density and location, its coordinates at a specific time step, or its association with a sink particle. In §3 we compare the numerical properties and computational

expense of the two schemes for laminar and turbulent flows.

Parallelization of the tracer methods has been implemented with MPI. The ATHENA source code including these passive tracer schemes can be pulled from the GitHub repository.¹

2.2.1 Velocity Field Tracers

ATHENA has previously been implemented with a particle-gas scheme for the study of protoplanetary disks. The particles are integrated using momentum feedback from the gas with a predictor-corrector method (Bai & Stone (2010)). However, if the particle’s interaction with the gas is disabled, they are effectively integrated using a first order in time scheme. We therefore implement second order in time passive particle schemes in ATHENA using a leap frog approach.

The velocity field tracers are assigned to a grid cell and are implemented as a doubly-linked list corresponding to each cell. These tracers are assigned coordinates within phase space and are integrated based on the underlying fluid velocity interpolated to the location of the particle. These tracers are initially uniformly distributed throughout the grid cell, using the GSL Mersenne twister PRNG² to assign randomized position. After the integration step tracers are transferred to the linked-list corresponding to the grid cell of their current location. This allows for efficient output of grid cell averaged tracer quantities.

Lower Order Method

We implement the velocity field tracers using two integration methods, both of which are effectively second order in time. In the lower order integration scheme, during the integration step the velocity of the underlying fluid at the current time, v^n , is

¹https://github.com/epaul626/athena_starparticle_tracers

²https://www.gnu.org/software/gsl/manual/html_node/Random-number-generator-algorithms.html

interpolated to the particle's current position, x^n . This is performed using a triangular shaped cloud (TSC) weighting function. If the tracer has current position x^n corresponding to grid cell i , the weighting is performed such that

$$\begin{aligned} w_{i-1} &= 0.5(1-d)^2 \\ w_i &= 0.75 - (d-0.5)^2 \\ w_{i+1} &= 0.5d^2. \end{aligned} \tag{2.8}$$

where d is the x coordinate of the particle in units of Δx and w_{i-1} , w_i , and w_{i+1} correspond to the weights for the left, current, and right grid cells. Using TSC weighting, the velocity field interpolation is second order in space. These weights are used to calculate the interpolated velocity at the current position, $v(x^n)$, and at the predicted position, $v(x^{n+1/2})$. The predicted position is calculated as

$$x^{n+1/2} = x^n + 0.5\Delta t v^n(x^n). \tag{2.9}$$

v^n and v^{n+1} are then interpolated to the predicted position using TSC weighting. The position of the tracer is iterated forward in time using the average velocity over the time step, $1/2(v^n + v^{n+1})$, interpolated to the predicted position at $t^{n+1/2}$,

$$x^{n+1} = x^n + 0.5\Delta t v^n(x^{n+1/2}) + 0.5\Delta t v^{n+1}(x^{n+1/2}). \tag{2.10}$$

Since the tracer integration takes place after the fluid velocity has been updated, we store v^n and use the newly calculated v^{n+1} to integrate the particles.

Higher Order Method

The higher order scheme similarly uses TSC weighting to interpolate the fluid velocity. It is slightly computationally more expensive as it requires the interpolation of both

v^n and v^{n+1} to x^n in order to calculate the predicted position,

$$x^{n+1/2} = x^n + 0.5\Delta t (0.75 v^n(x^n) + 0.25 v^{n+1}(x^n)). \quad (2.11)$$

The particle is integrated from its predicted position as,

$$x^{n+1} = x^{n+1/2} + 0.5\Delta t (0.25 v^n(x^{n+1/2}) + 0.75 v^{n+1}(x^{n+1/2})). \quad (2.12)$$

After x^{n+1} is calculated for each particle using one of these integration schemes, if x^{n+1} lies outside of the bounds of the previous grid cell the particle will be popped off of its current list and onto the list corresponding to its new grid cell. Boundary conditions are treated similarly.

2.2.2 Monte Carlo Tracer Particles

We also implement a Monte Carlo tracer method in ATHENA, a novel tracer method first implemented in AREPO (Genel et al. (2013)). These Monte Carlo tracers are not given coordinates within the grid but are simply assigned to a grid cell. To track mass fluxes between cells, a subset of tracers is elected and reassigned to neighboring cells. This introduces some additional numerical noise, as we will show in §3. This tracer particle scheme has been applied to cosmological hydrodynamic simulations to investigate gas accretion onto galaxies. It has been suggested that the Monte Carlo method more correctly reproduces the mass distribution of astrophysical fluids, especially in the presence of shocks and turbulent environments, as the velocity field method does not necessarily behave according to the solution to the Riemann problem at cell interfaces (Genel et al. (2013)). It has been shown that while velocity field tracers do not accurately follow converging flows and tend to concentrate in halo centers in cosmological simulations, Monte Carlo tracer particles do not exhibit this bias (Nelson et al. (2013)).

We implement our Monte Carlo tracers using a 3-dimensional grid of linked lists, each list corresponding to a grid cell. If a tracer needs to be transferred from one grid cell to a neighboring grid cell, it is simply popped of the previous grid cell's linked list and pushed onto the current grid cell's linked list. Because the tracers are implemented as their own grid, cell-averaged quantities for the properties stored in the passive tracers can be outputted efficiently.

At each time step the probability for tracer particle transfer between cells with mass M_i^n and M_{i+1}^n is calculated from the mass flux in the i direction, $\Delta M_{i,i+1}^n$, calculated by the van Leer integrator, and the mass M_i^n , the mass contained within a grid cell before the cell-centered density is updated.

$$p_{i,i+1} = \frac{\Delta M_{i,i+1}^n}{M_i^n}. \quad (2.13)$$

The particle integration step occurs after the cell-centered grid variables are updated using the 3-dimensional fluxes. For each tracer within a grid cell's linked list, a pseudo-random number, p , is generated using the GSL Mersenne twister generator. If $p \leq p_{i,i+1}$, the tracer is transferred from cell i to cell $i + 1$. The integration step is performed for each of the 3 spatial directions. Refer to Figure 2.1 for illustration.

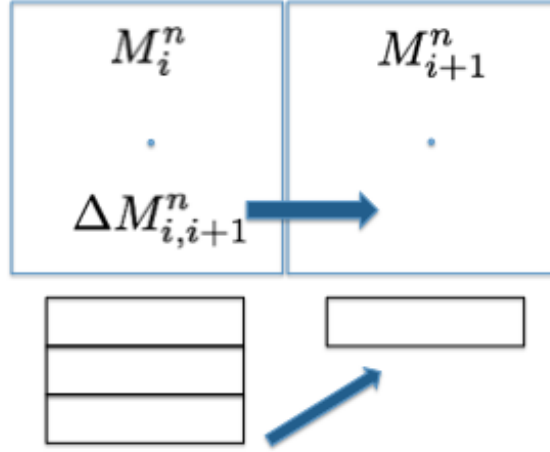


Figure 2.1: A schematic demonstrating the implementation of Monte Carlo tracers in ATHENA. Tracers are implemented in linked lists for each grid cell. The probability of transfer between neighboring linked lists i and $i + 1$ is $p_i = \frac{\Delta M_{i,i+1}}{M_i}$.

2.3 Sink Particles in ATHENA

The use of sink particles becomes necessary in the study of the long-term evolution of a system under gravitational collapse, such as in the study of the evolution of turbulent star formation. As many dense pre-stellar cores develop within a molecular cloud, the density contrast within a simulation volume can reach values as high as 10^6 . As collapse continues the radius of the protostar may fall below the grid refinement and its profile cannot be resolved using a grid-based code. The time step set by the CFL condition will decrease drastically, making it unfeasible to follow further evolution of star formation within the simulation volume.

Sink particles have been implemented in ATHENA in order to allow one to follow the long-term evolution of collapse. Sink particles are created as motivated by the Larson-Penston density profile,

$$\rho_{LP}(r) = \frac{8.86c_s^2}{4\pi Gr^2}. \quad (2.14)$$

This is a well known solution for the density profile of the collapse of a gravitationally-unstable isothermal sphere and has been numerically shown to lead to core collapse (Larson (1969), Penston (1969)). If the density exceeds the value of ρ_{LP} for $r = \Delta r/2$, a cell is flagged as possibly requiring a sink particle. In addition to the density threshold check, other requirements are that the central cell is a gravitational potential minimum, the control volume is surrounded by a converging flow ($\nabla \cdot v < 0$), and the control volume is gravitationally bound ($E_{grav} + E_{th} + E_{kin} < 0$).

After the creation of a sink particle, a control volume of size $(3\Delta x)^3$ is created surrounding the sink particle. Sink particles velocities and positions are integrated in time using the leapfrog method using the gravitational field interpolated to the particle's location using TSC weighting (Gong & Ostriker (2013)). We implement our passive tracer particles such that if one falls within the control volume of a given sink particle the corresponding tracer particle is identified with the sink particle. The user can select to output only the properties of tracers identified within sink particles.

Chapter 3

Evaluation of Tracer Methods

We set up several test problems in order to evaluate the computational performance and validity of our passive tracer methods in comparison to the underlying fluid density.

3.1 Advection of a Circle

We begin with a very simple problem of the advection of a circle at uniform velocity. We initialize a 100×100 periodic grid with a background density $\rho = 1$ and a central circular region with $\rho = 2$. The entire volume is given $v_x = 1$ and uniform pressure $P = 1$. We apply an adiabatic equation of state with $\gamma = 5/3$, giving us $c_s = \sqrt{\frac{\gamma P}{\rho}} = \sqrt{5/3}$ in the background region.

We distribute the tracers such that the number of tracers per cell is proportional to the underlying fluid density, $n_{tracer} = \alpha\rho$. We run each test for 200 cycles, the time needed for the circle to cross the simulation volume twice, and compare the tracer density to the fluid density and the evolution of the structure of the density field.

We display the fluid density and tracer density at cycle 200 in Figures 3.1 and 3.2. The pseudocolor images of tracer density are plotted using the number of tracers per grid cell normalized to the fluid density, n_{tracer}/α . Here the passive tracers are

initialized such that $\alpha = 5$. We see that both the fluid density and Monte Carlo tracer density diffuses in the direction of advection. However, both the higher and lower order velocity field tracers are less diffusive than the fluid density. Even in the uniform background region the Monte Carlo tracers exhibit much statistical noise, with enhanced diffusion over the fluid density. As noted by Genel et al. (2013), this can be explained because the Monte Carlo tracers are spread out over the grid cell and do not undergo a reconstruction step. This can allow a tracer that enters one face of a grid cell to immediately exit the opposite face and ‘overtake’ other tracers.

Both the higher and lower order velocity field tracer methods exhibit a ‘pulsing’ behavior between alternating cycles, as can be seen in Figure 3.3. This is because a discrete number of tracers is uniformly distributed throughout a given grid cell. As the circle is advected, the fluid density and velocity profiles are diffused in the direction of advection. As the tracer density profile comes in and out of phase of the grid cell boundaries, we see this pulsing behavior appear in the velocity field tracer density, as we are outputting the number of tracers within a grid cell rather than the coordinates of individual tracers within a cell.

We evaluate the noise of the tracer density with respect to the fluid density in Figure 3.4. Here we define the normalized noise, σ_{tracer} , as

$$\sigma_{tracer}^2 = \frac{\sum_i (\alpha \rho_i - n_{tracer,i})^2}{\sum_i (\alpha \rho_i)^2} \quad (3.1)$$

where the sum is performed over all grid cells at one time step.

Both velocity field tracer methods appear to maintain a constant low statistical noise with increasing tracer density in the case of a uniform velocity field. We see that the noise of the Monte Carlo tracer density with respect to the fluid decreases approximately as $\sigma_{tracer} \sim \langle n_{tracer} \rangle^{-0.5}$.

In Figure 3.5 we display the evolution of σ_{tracer} over 300 cycles during the uniform

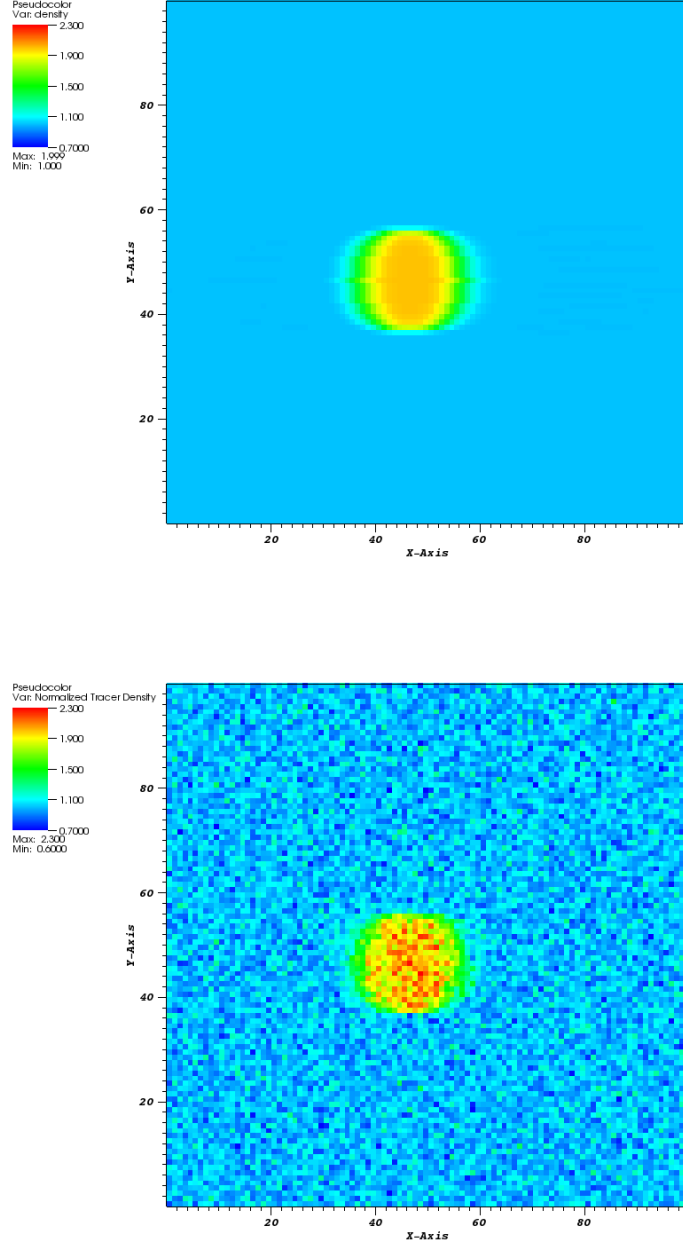


Figure 3.1: Pseudocolor images of fluid density, ρ , (top) and normalized tracer density, n_{tracer}/α , using Monte Carlo scheme (bottom). The fluid and tracers are initialized with a background of $\rho = n_{tracer}/\alpha = 1$ and central region $\rho = 2$. Tracers are initialized such that $\alpha = 5$.

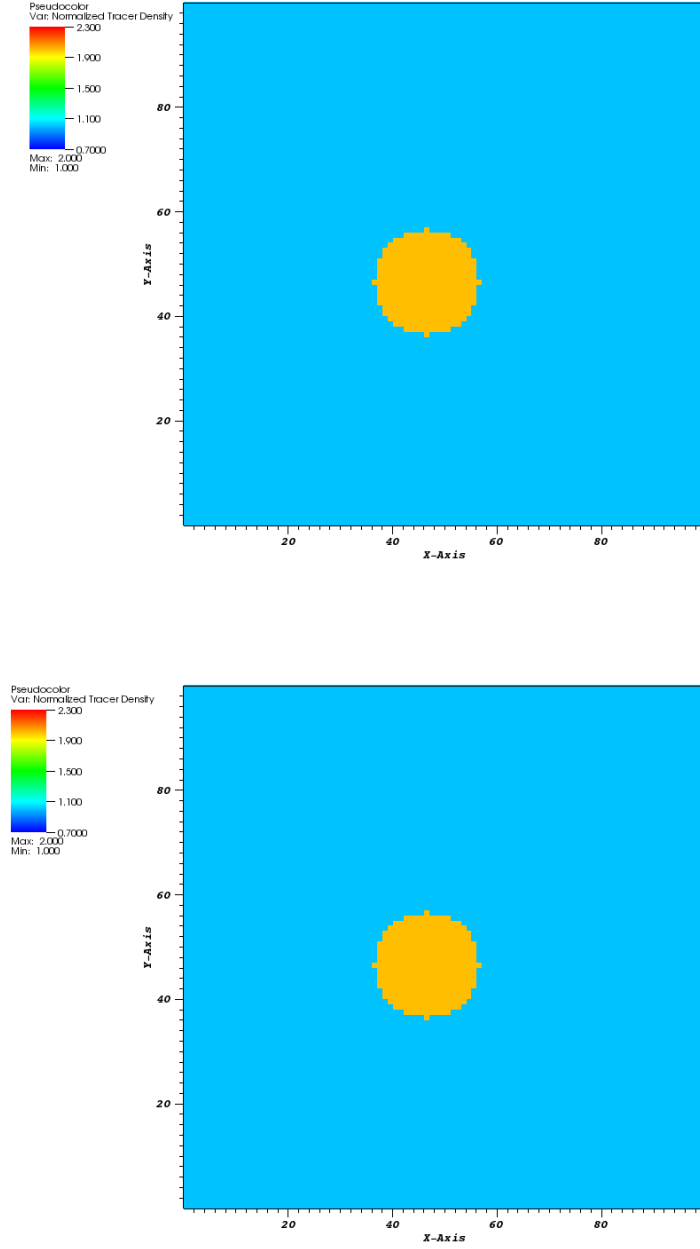


Figure 3.2: Pseudocolor images of normalized tracer densities, n_{tracer}/α , for the lower order (top) and higher order (bottom) velocity field tracer schemes. The fluid and tracers are initialized with a background of $\rho = n_{tracer}/\alpha = 1$ and central region $\rho = 2$. Tracers are initialized such that $\alpha = 5$.

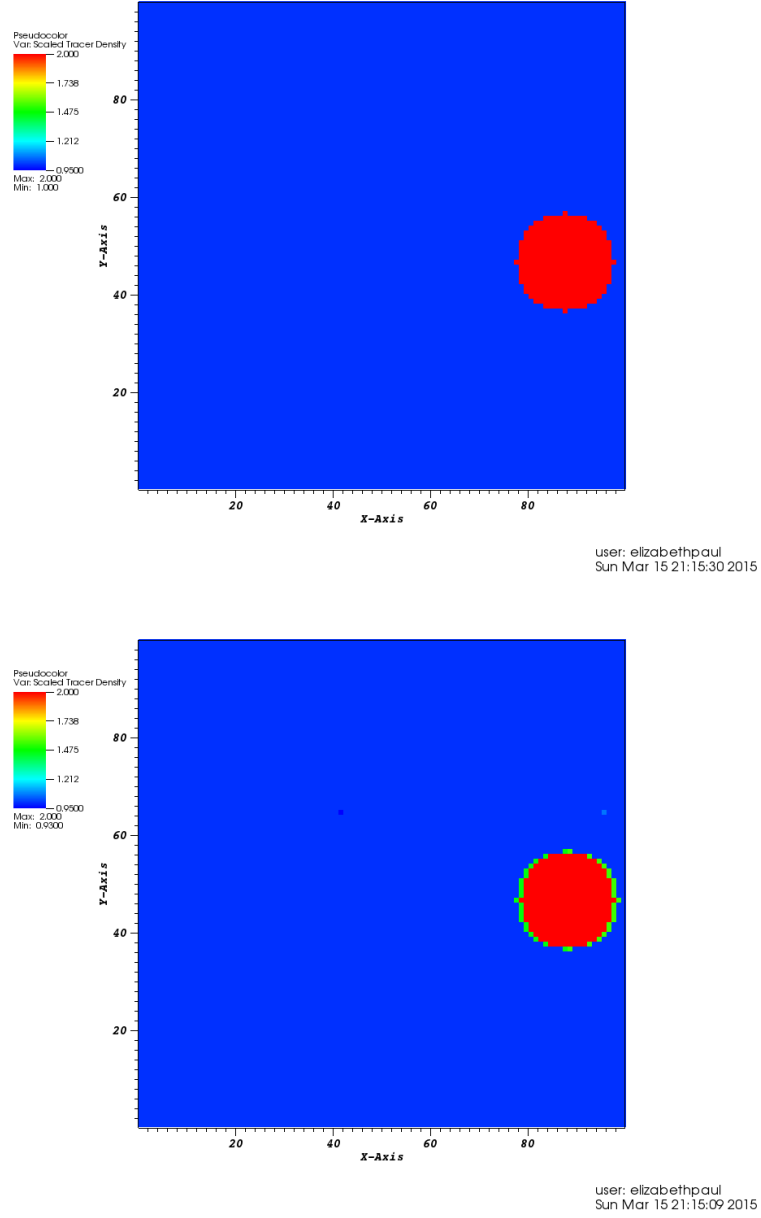


Figure 3.3: Pseudocolor images of subsequent cycles of the 2-dimensional advection of a circle test. The higher order velocity field tracer normalized density, n_{tracer}/α , is shown.

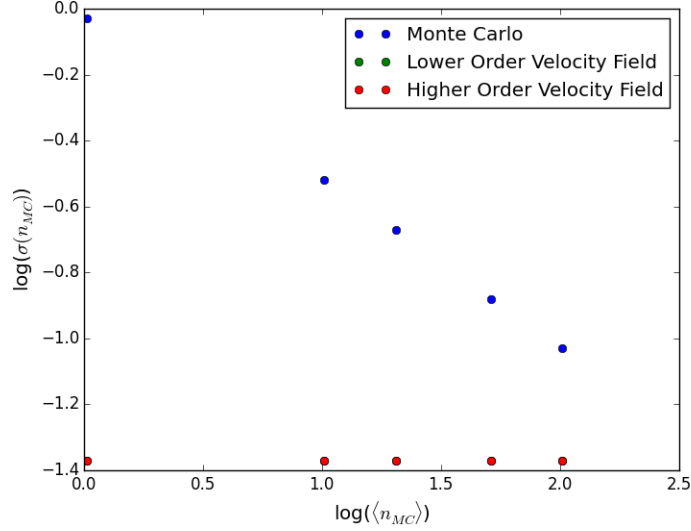


Figure 3.4: The noise of the tracer density with respect to the fluid density (Eq. 3.1) calculated for all grid cells, $\sigma(n_{tracer})$, is shown for increasing number of tracers per cell, $\langle n_{tracer} \rangle$, for the 2-d advection of a circle test.

advection test initializing tracers with $\alpha = 100$. Only the higher order velocity field tracer method is shown as the lower order method performed very similarly. We see the oscillations of the noise of the velocity field tracers due to the ‘pulsing’ effect described earlier. The noise of the velocity field method slowly increases over time while that of the Monte Carlo tracers reaches a plateau after about 50 cycles.

Although the Monte Carlo tracer method is much noisier than the velocity field method even for a simple advection test, in Figure 3.6 we see that this method is much less computationally expensive. While t_{run} appears to scale similarly with N_{tracer} for both Monte Carlo and velocity field methods, the runtime for the Monte Carlo method is consistently $\sim 6 - 7$ times less expensive. This could be because for both the velocity field and Monte Carlo method the tracer integration step requires iterating over the grid of linked list. However, the Monte Carlo method computational time is dominated by pseudo-random number generation while the velocity field method is dominated by the interpolation step. At each time step the higher order method requires an extra TSC weighting calculation over the lower order method to interpo-

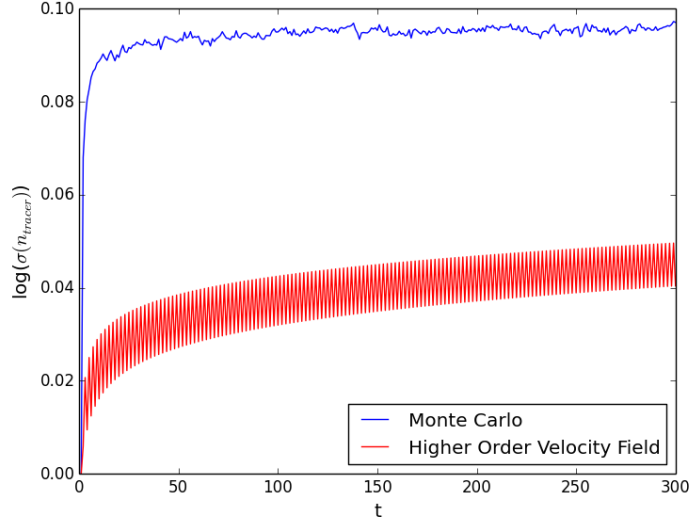


Figure 3.5: The time evolution of the noise of the tracer entity with respect to the fluid density, $\sigma(n_{tracer})$, is shown for the higher order velocity field and Monte Carlo passive tracer methods. Tracers are initialized such that the number per cell is proportional to the fluid density in that cell, $n_{tracer} = 100\rho$. t is the cycle number of the simulation.

late v^{n+1} to the tracer position. Since the higher order method does not significantly decrease the noise over the lower order scheme, it would be advisable to use the lower order method in the case of simple advection.

With reference to Figure 3.4, it appears that σ_{tracer} for the Monte Carlo method would decrease to the level of σ_{tracer} for the velocity field method for $\log(\langle n_{tracer} \rangle) \sim 2.5$ or $\log(N_{tracer}) \sim 6.5$. With reference to Figure 3.6, if we extrapolate the cost for this value of N_{tracer} , the Monte Carlo method would be ~ 7 times less expensive than the velocity field method. In the case of uniform advection, the noise level of the velocity field schemes remains small as N_{tracer} decreases, thus it would be advantageous to use this method over the Monte Carlo method. However, as we will discuss in §3.2, this is not the case for more complex velocity fields.

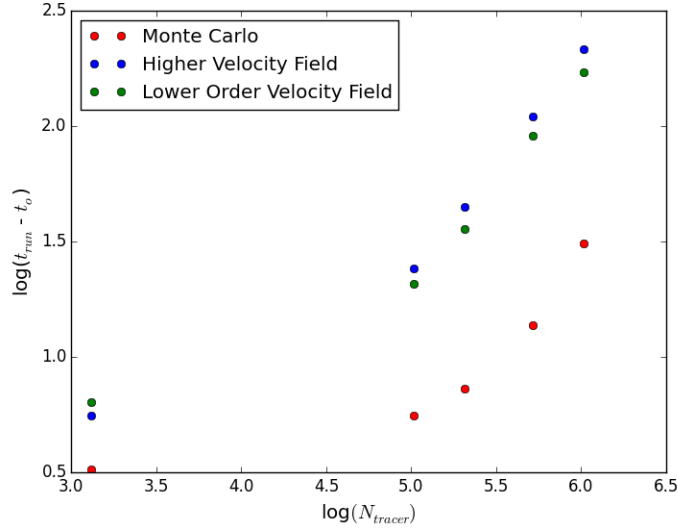


Figure 3.6: The computational time in seconds, $(t_{run} - t_0)$, is calculated for increasing number of total tracers, N_{tracer} , for the 2-dimensional advection of a circle problem, where t_0 is the runtime without passive tracers.

3.2 Blast Wave

We furthermore test the performance of our passive tracer methods in the presence of strong shocks using a 2-dimensional MHD blast wave problem, adapted from the problem as described in Stone et al. (2008). We initialize a periodic 100×100 grid with a uniform density $\rho = 1$. The background ambient medium is given $P = 0.1$ and a central circular over-pressured region is given $P = 10$. An initial magnetic field $\mathbf{B} = 10$ is inclined at 45° with respect to the x axis.

In Figures 3.7 and 3.8 we display the fluid density and tracer number per cell n_{tracer} , at $t = 0.2$. The pseudocolor images of tracer density are plotted using the number of tracers per grid cell normalized to the fluid density, n_{tracer}/α . Here the passive tracers are initialized such that $\alpha = 20$. In both of the velocity field methods we see the development of numerical wave-like structure in the central under-dense region. However, both the higher and lower order methods appear to preserve the shock-front structure fairly well. The spatial extent of the shock front in the Monte Carlo scheme is noticeably larger than that of the fluid density. Thus in the case

that one would like to accurately trace the evolution of structure over time it may be advisable to employ the velocity field method.

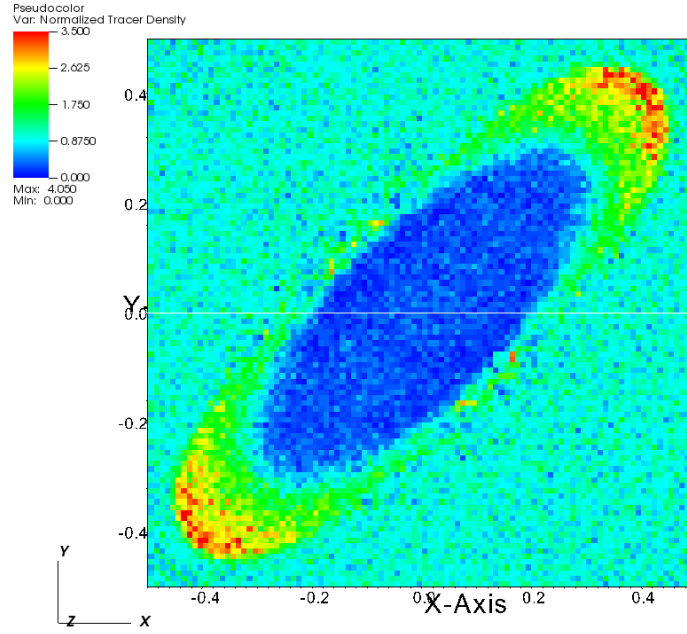
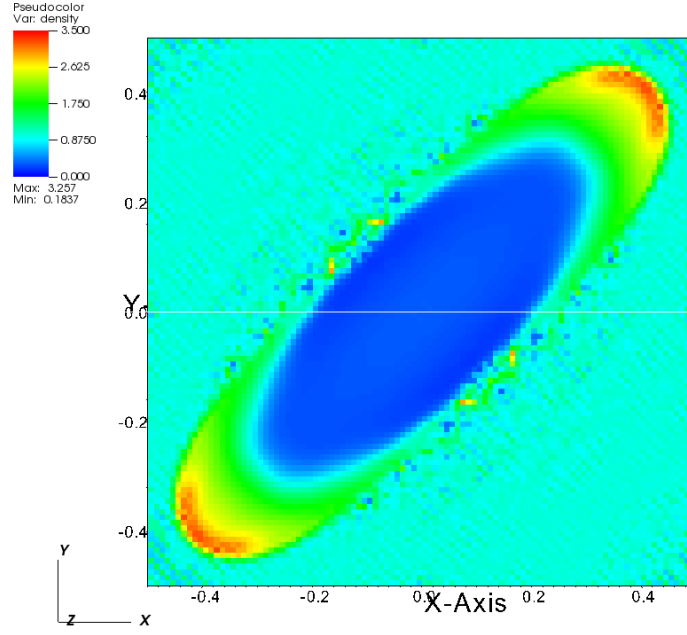


Figure 3.7: Pseudocolor images of fluid density, ρ , (top) and normalized tracer density, n_{tracer}/α , for the Monte Carlo scheme (bottom). The images are shown at $t = 0.2$ for the 2-dimensional MHD blast wave test. The tracers are initialized such that the number of tracers per cell is proportional to the fluid density, $n_{tracer} = \alpha\rho$, where $\alpha = 20$.

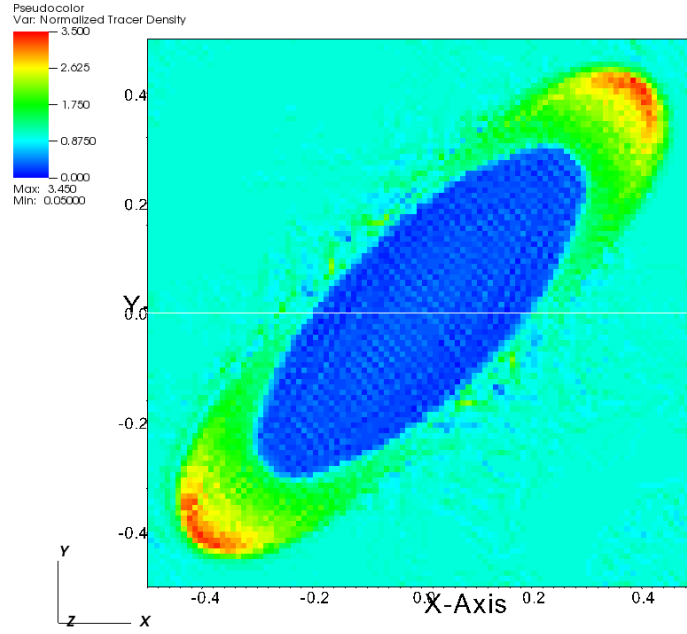
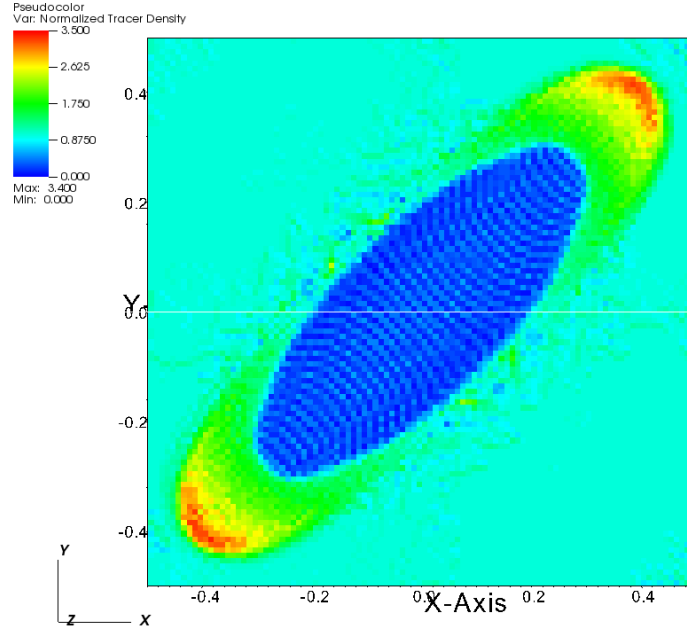


Figure 3.8: Pseudocolor images of the normalized tracer densities, n_{tracer}/α , for the lower order (top) and higher order (bottom) velocity field schemes. The images are shown at $t = 0.2$ for the 2-dimensional MHD blast wave test. The tracers are initialized such that the number of tracers per cell is proportional to the fluid density, $n_{tracer} = \alpha\rho$, where $\alpha = 20$.

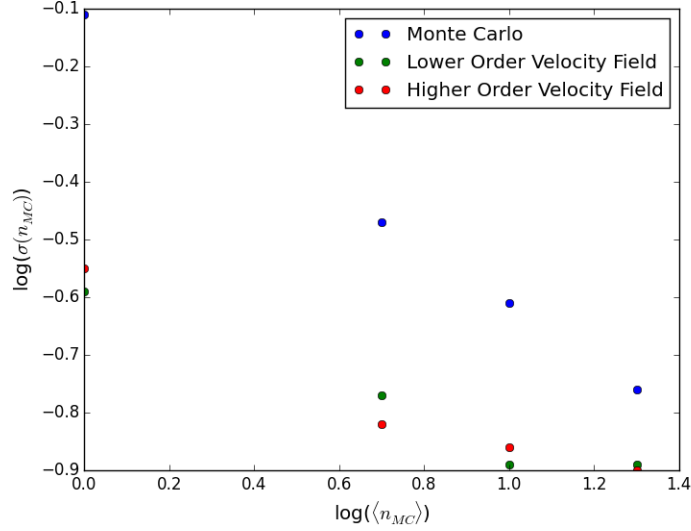


Figure 3.9: The noise of the tracer density with respect to the fluid density, $\sigma(n_{tracer})$, is shown for increasing number of tracers per cell $\langle n_{tracer} \rangle$. The noise (Eq. 3.1) is calculated for all grid cells at $t = 0.2$ of the 2-dimensional MHD blast wave test.

In Figure 3.9 we see that again $\sigma(n_{tracer}) \sim \langle n_{tracer} \rangle^{-0.5}$ for the Monte Carlo scheme. The velocity field methods appear to perform similarly to each other, with about a $\sim 30\%$ decrease in overall noise over the Monte Carlo scheme at the highest tracer density. However, in Figure 3.10 we see that this improvement in reproducing the fluid density field comes with a significant computational cost. With $N_{tracers} = 2 \times 10^5$, t_{comp} of the velocity field scheme is increased by a factor of 3 over the Monte Carlo method. However, if one desires to follow the evolution of a structure such as a dense core, it may be feasible to initialize velocity field tracers only within this select region without a prohibitive computational cost.

In view of Figure 3.9, we see that the noise level for the passive tracer schemes is similar, $\sigma(n_{tracer}) \sim 0.17$, for number of Monte Carlo tracers per cell $\langle n_{tracer} \rangle \sim 20$ and number of velocity field tracers per cell $\langle n_{tracer} \rangle = 5$. In view of Figure 3.10, we see that at these number densities the computational time for the Monte Carlo method and velocity field method are similar. We note that t_{run} for the Monte Carlo method is consistently ~ 3 times less expensive than the velocity field methods for a

given N_{tracer} .

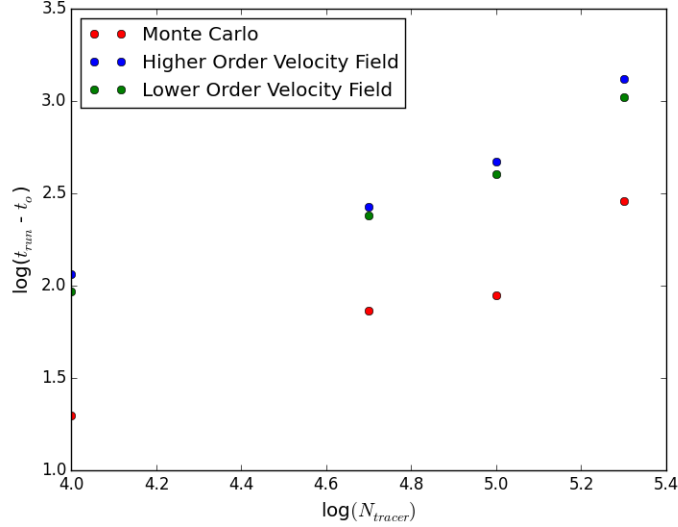


Figure 3.10: The computational time in seconds, $(t_{run} - t_0)$, is calculated for increasing number of total tracers, N_{tracer} , for the 2-dimensional MHD blast wave problem, where t_0 is the runtime without passive tracers.

3.3 Bonnor-Ebert Sphere

We test the interaction of our passive tracers with collapsed regions and sink particles using a 3D simulation of the evolution of a Bonnor-Ebert sphere. We adapt our problem from that described in Gong & Ostriker (2013). We initialize a sphere of radius slightly larger than the critical radius, $R \sim 1.1 R_{BE, crit}$ where

$$R_{BE, crit} = 0.274 c_s \left(\frac{G \rho_e}{\pi} \right)^{1/2}. \quad (3.2)$$

We initialize a periodic simulation volume with $L_x = L_y = L_z = 5.5 R$ and resolution 130^3 .

Since we ultimately want to apply our passive tracer methods to follow the collapse of dense cores within a GMC, this simulation represents a highly-idealized version of this situation. We initialize our tracers such that the number of tracers per cell is

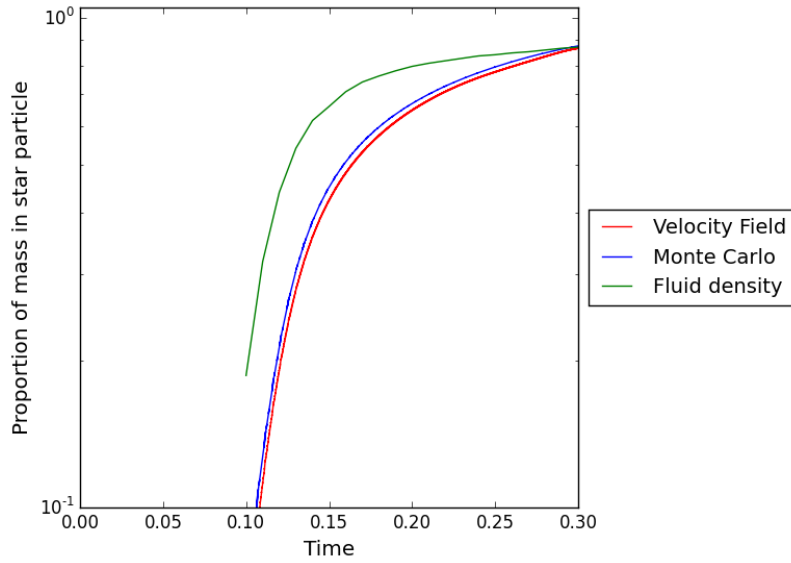


Figure 3.11: The proportion of total equivalent mass within the star particle in the stationary Bonnor-Ebert sphere problem is shown for the fluid density, Monte Carlo passive tracers, and lower-order velocity field tracers. Tracers are only initialized within the central sphere such that the number within a given cell is proportional to the fluid density, $n_{tracer} = 20\rho$.

proportional to the fluid density within the cell, $n_{tracer} = 20\rho$, only within the central sphere. We look at the total mass of tracers that fall within the sink region as collapse continues compared to the proportion of the fluid mass in the sink region.

In Figure 3.11, we see that the velocity field tracers and Monte Carlo tracers perform very similarly in following the collapse of the sphere. While at earlier times we see that a higher proportion of the fluid mass than the tracer mass lies within the sink region, as the sink particle is initialized with non-zero mass, by $t = 0.30$ the proportion of tracers within the sink region reaches the value for the fluid density. The performance of both of our passive tracer methods in this idealized case indicates that they may be robust in following the collapse in our subsequent simulations of turbulent molecular clouds.

Chapter 4

Turbulence Problem

We set up the decaying turbulent star formation problem using an isothermal equation of state, $P = \rho c_s^2$ with $c_s = 0.2 \text{ km s}^{-1}$, as temperature is observed to be relatively constant throughout GMCs (Dobbs et al. (2014)). The simulation volume ($L_x = L_y = L_z = 20 \text{ pc}$) is initially filled with a uniform density gas with H number density $n = 100 \text{ cm}^{-3}$ and periodic boundary conditions.

The turbulent velocity perturbations are generated using a power spectrum such that

$$E(k) \sim |\delta \mathbf{v}_k^2| \propto k^{-4}. \quad (4.1)$$

This corresponds to current observations of the size-linewidth relation, as discussed in § 1.4, as

$$\sigma_v^2 \sim E(k) \sim \int k^{-4} d^3k \quad (4.2)$$

$$\sigma_v \sim k^{-1/2} \sim L^{1/2}. \quad (4.3)$$

The amplitude of the perturbations are drawn for wavenumber such that $2\Delta x \leq \frac{2\pi}{k} \leq \frac{L}{2}$. The velocity perturbations are summed over the simulation volume and the mean perturbation in each direction, $\langle \delta v \rangle$, is subtracted off such that the net

momentum of the gas vanishes ($\int \rho \delta \mathbf{v} = 0$). The non-solenoidal component of the velocity perturbations is projected off such that the perturbations are incompressive ($\nabla \cdot \delta \mathbf{v} = 0$), and the perturbations are applied at the initial time step and then are allowed to evolve and decay. The application of velocity perturbations in this manner is consistent with observations of molecular clouds (Stone et al. (1998)).

The velocity perturbation amplitudes, $|\delta v_k|$, are set by scaling the kinetic energy relative to a characteristic gravitational energy,

$$E_{kin} = 0.5 \alpha_{vir} E_{grav}, \quad (4.4)$$

where

$$E_{grav} = \frac{3GM_{GMC}^2}{5R_{GMC}}. \quad (4.5)$$

Here M_{GMC} is the total mass contained within the simulation volume and $R_{GMC} = L/2$. Note that for our simulation domain with periodic boundary conditions, Equation 4.5 does not give the actual value of the gravitational energy. Instead, it is used to define a typical value of kinetic energy that a realistic cloud would have at a scale comparable to L . The rms turbulent velocity, $\langle v_{turb} \rangle$, is given by

$$\langle v_{turb} \rangle = (2\langle E_{kin} \rangle / M_{GMC})^{1/2} = (\alpha_{vir} E_{grav} / M_{GMC})^{1/2}. \quad (4.6)$$

from which we can define the Mach number, $\mathcal{M} = \langle v_{turb} \rangle / c_s$. We vary α_{vir} in our simulations to study the effect of increased turbulent motions on the collapse of dense cores during star formation.

4.1 Evaluation of Passive Tracer Method with Turbulence Problem

Before applying our passive tracer method to follow the collapse of dense cores within GMCs in our turbulence simulation, we want to first evaluate the robustness of our passive tracers. We do this by initializing the turbulence problem with initial tracer number per grid cell $n_{tracer} = 1$ and $n_{tracer} = 5$ and evaluate the statistical noise compared to the fluid density before global collapse occurs. We can also visually compare the structure in the fluid density and tracer number density throughout the simulation.

The simulation was initialized with $\alpha_{vir} = 1$, giving us an initial $\mathcal{M} = 13.36$. The initial fluid density is 100 cm^{-3} and the tracers are initialized such that the number of tracers per grid cell is proportional to the fluid density in the cell, $n_{tracer} = \alpha \rho$ where $\alpha = 0.01$ and 0.05 . In §4.1.1 and §4.1.2 we present pseudocolor images of the fluid column density, integrated over the x dimension. The tracer column density has been scaled such that it is comparable to the fluid column density. At later times we also show the star particle positions overlaid on the column density, with color mapped to star particle masses.

4.1.1 $n_{tracer} = 1$

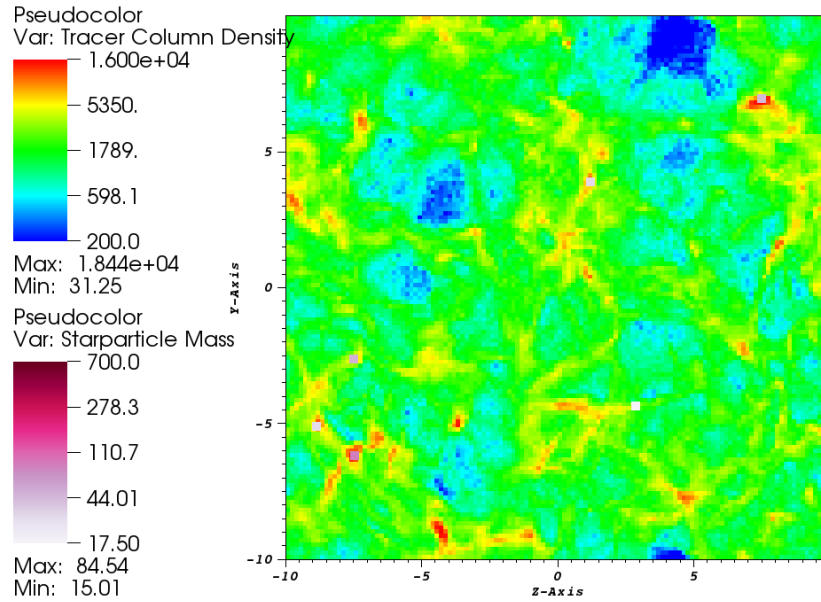
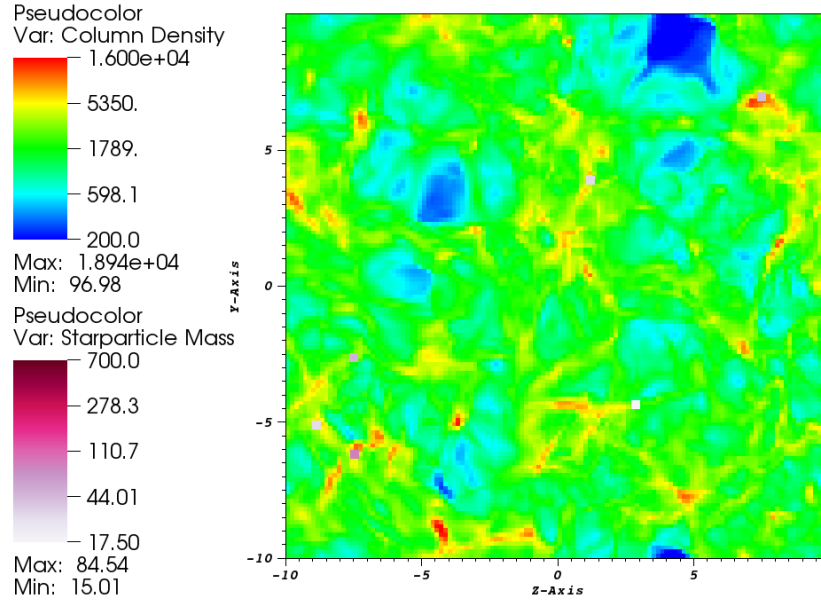


Figure 4.1: Pseudocolor images of the column density ($\text{pc cm}^{-3} = 3.1 \times 10^{18} \text{ cm}^{-2}$) of the fluid (top) and scaled tracer density (bottom), at $t = 2.5$ Myr. Tracers are initialized uniformly such that the number per cell, $n_{\text{tracer}} = 1$, and the initial fluid density is $n_0 = 100 \text{ cm}^{-3}$. Star particles are overlaid with color mapped to stellar mass (M_\odot).

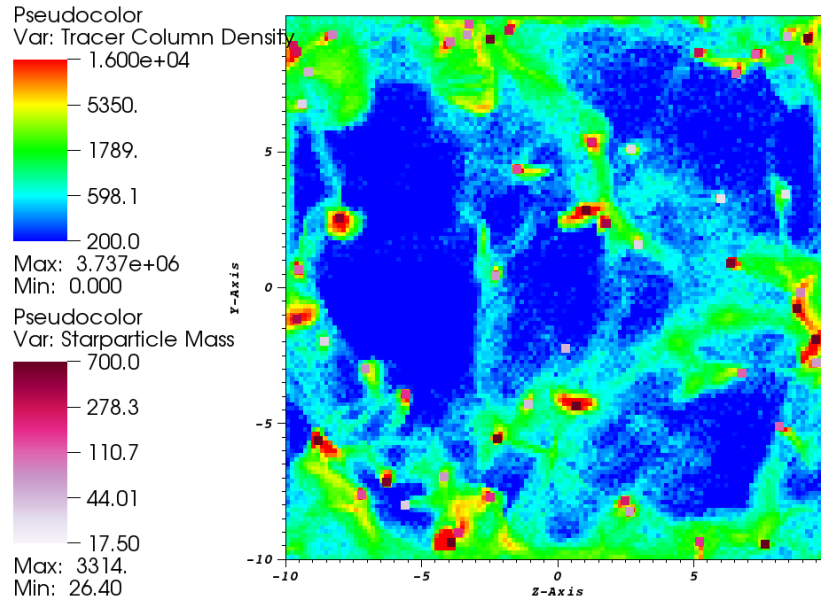
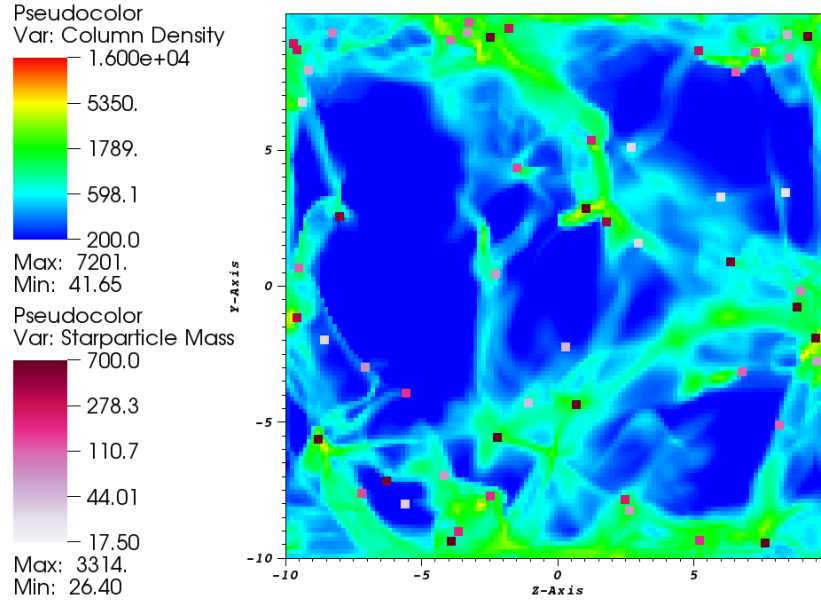


Figure 4.2: Pseudocolor images of the column density ($\text{pc cm}^{-3} = 3.1 \times 10^{18} \text{ cm}^{-2}$) of the fluid (top) and scaled tracer density (bottom), at $t = 11.0$ Myr. Tracers are initialized uniformly such that the number of tracers per cell, $n_{\text{tracer}} = 1$, and the initial fluid density is $n_0 = 100 \text{ cm}^{-3}$. Star particles are overlaid with color mapped to stellar mass (M_{\odot}).

4.1.2 $n_{tracer} = 5$

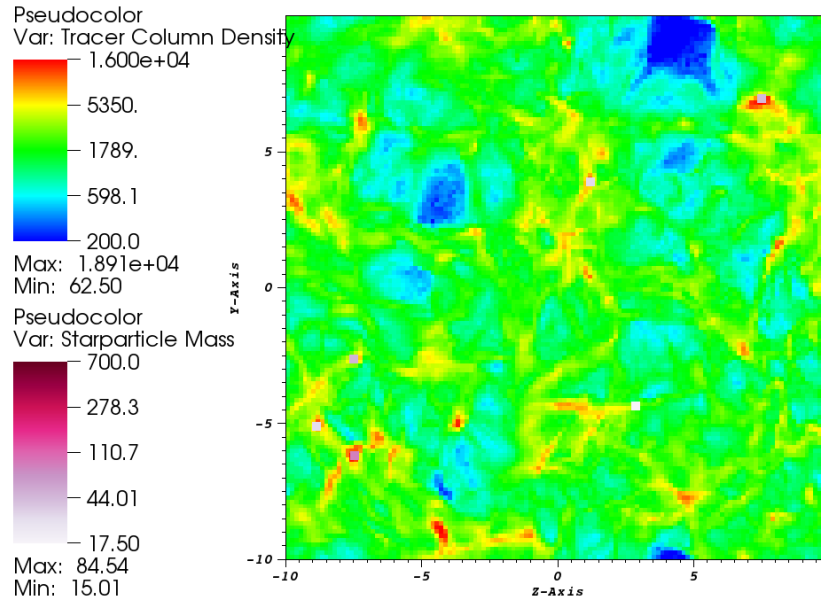
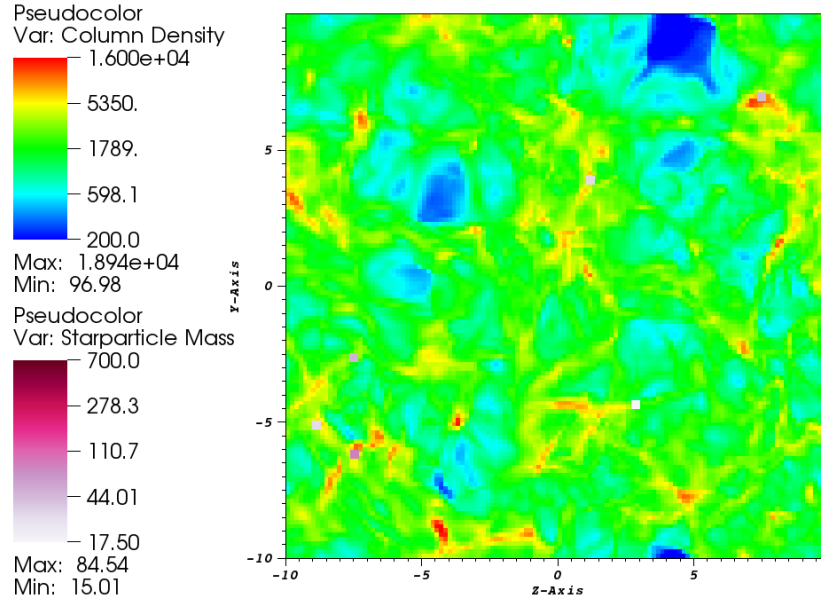


Figure 4.3: Pseudocolor images of the column density ($\text{pc cm}^{-3} = 3.1 \times 10^{18} \text{ cm}^{-2}$) of the fluid (top) and scaled tracer density (bottom), at $t = 2.5$ Myr. Tracers are initialized uniformly such that the number of tracers per cell, $n_{\text{tracer}} = 5$, and the initial fluid density is $n_0 = 100 \text{ cm}^{-3}$. Star particles are overlaid with color mapped to stellar mass (M_{\odot}).

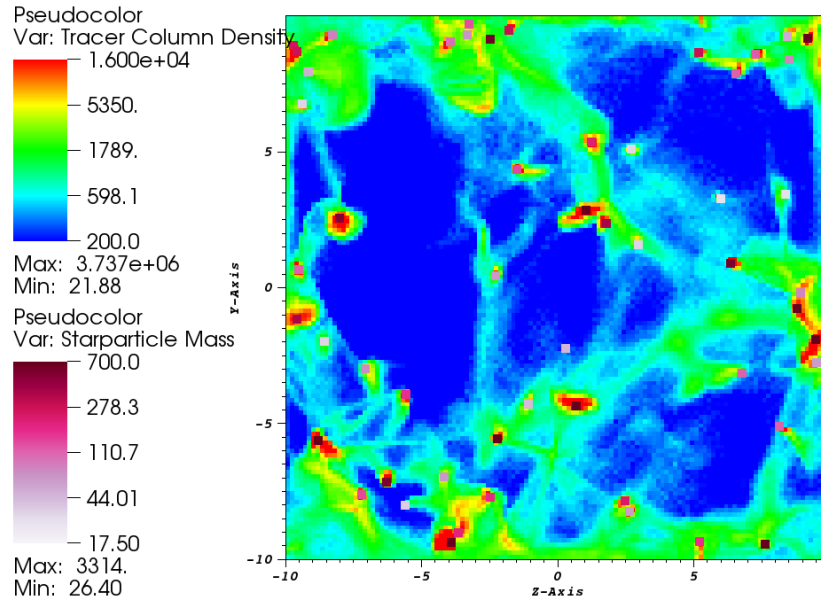
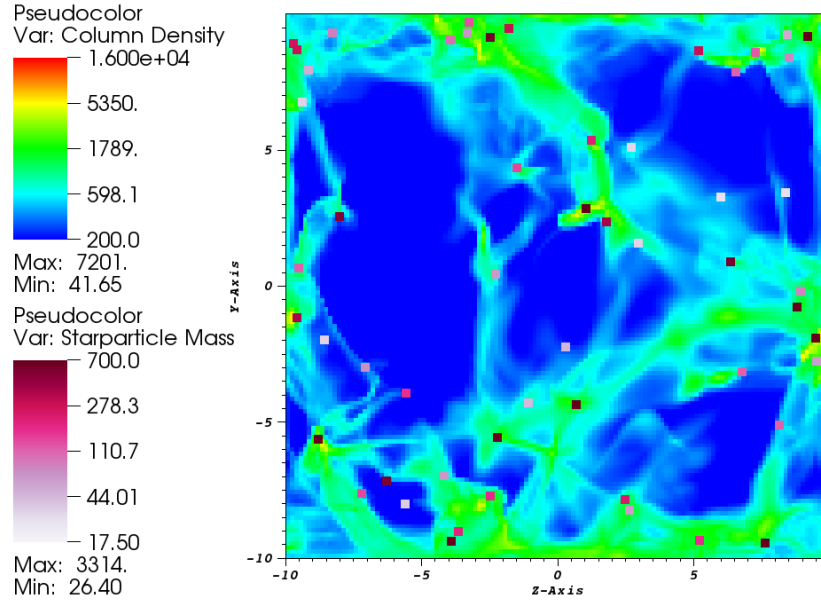


Figure 4.4: Pseudocolor images of the column density ($\text{pc cm}^{-3} = 3.1 \times 10^{18} \text{ cm}^{-2}$) of the fluid (top) and scaled tracer density (bottom), at $t = 11.0$ Myr. Tracers are initialized uniformly such that the number of tracers per cell, $n_{\text{tracer}} = 5$, and the initial fluid mass density is $n_0 = 100 \text{ cm}^{-3}$. Star particles are overlaid with color mapped to stellar mass (M_\odot).

By visual comparison between the fluid column density and scaled tracer column density, we can see that the tracers appear to reconstruct the fluid density field reasonably well. With reference to the pseudocolor images at the later times after the turbulence has developed, the tracer particles accumulate in the regions surrounding the star particles, as they continue to be integrated after falling within a sink region. However, we see that the filamentary structures and over-dense cores in the fluid column density are traced well throughout the simulation. There does not appear to be an appreciable difference between the results for $n_{tracer} = 1$ and $n_{tracer} = 5$.

In addition to simple visual comparison of the performance of our passive tracer method, we can quantify the statistical noise of the tracer number per cell in comparison to the fluid density using the same metric defined in §3,

$$\sigma_{tracer}^2 = \frac{\sum_i (\alpha \rho_i - n_{tracer,i})^2}{\sum_i (\alpha \rho_i)^2}, \quad (4.7)$$

where α is the proportionality constant between n_{tracer} and ρ .

In Figure 4.5 we show the evolution of this metric until $t = 2$. At later times after gravitational collapse has set in and sink regions have formed, we see that tracer particles tend to accumulate around the sink regions and a simple calculation of this noise would not be informative. While σ_{tracer} is somewhat higher than that calculated for the idealized problems in §3, it decreases by a factor of about 2 with an increase to $n_{tracer} = 5$.

For most applications it is not necessary to track the evolution of the entire simulation volume using tracer particles. For the study of turbulent star formation, we would like to follow the evolution of dense cores. Since we only choose to place tracers in a fraction of the simulation volume, it is much more computationally feasible to initialize tracers at a higher number per cell and thus trace the evolution of fluid with greater precision. At $n_{tracer} = 1$ with a resolution of 128^3 there were a total of 2×10^6

tracers initialized, with a computational time of 32000 seconds. At $n_{tracer} = 5$ there were a total of 10^7 tracers with a total computational cost of 39000 seconds, while a comparable simulation without tracers has a runtime of 28000 seconds. Thus we see that even with a very large number of tracers, the computational time is increased by $\sim 15 - 40\%$ with the Monte Carlo method. We note that the computational time per passive tracer is reduced from 0.002 seconds for $n_{tracer} = 1$ to 0.001 seconds for $n_{tracer} = 5$. This may imply that the pseudo-random number generation for each tracer is a small part of the cost, and that the scaling of tracer cost depends more on the number of zones than the number of tracers. This may be because each integration step requires iterating over the grid of linked lists of tracers. However, memory costs go up with the number of tracers.

In the following simulations in Chapter 5 we initialize $\sim 6 \times 10^7$ tracers but with much higher resolution. While in these tests we had one tracer equivalent to a mass of $\sim 1.3 \times 10^{-2} M_{\odot}$, in the following simulations each tracer will trace an equivalent mass of $\sim 1.3 \times 10^{-4} M_{\odot}$, so we can expect the statistical noise to be much lower than that observed in these tests.

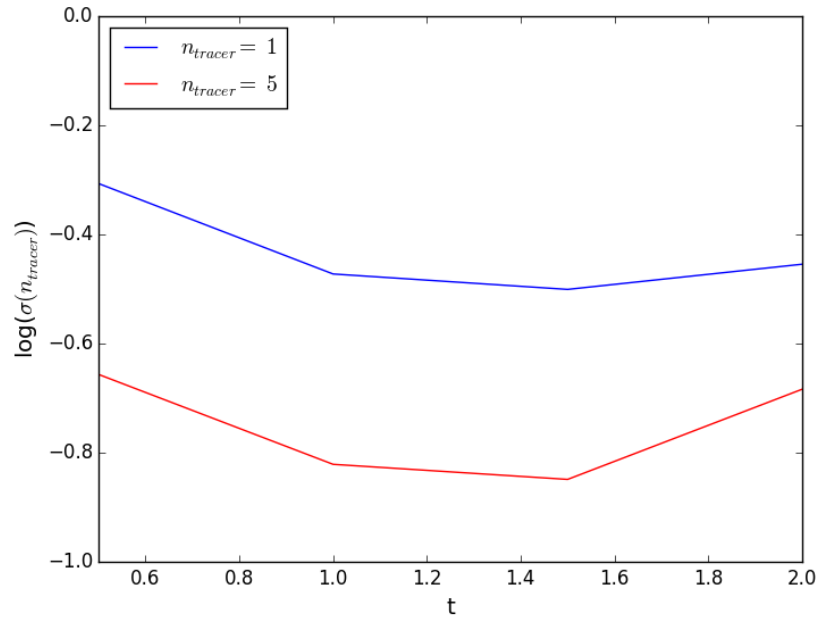


Figure 4.5: The normalized noise, σ_{tracer} , of the passive tracers in comparison to the fluid density for the turbulence problem initialized with uniform tracer number per cell, $n_{tracer} = 1$ and 5. Time is given in code units, $[t_{code}] = 0.98$ Myr.

Chapter 5

Turbulent Star Formation with Tracers - Results

5.1 Parameterization

In order to follow the collapse of dense cores as a GMC collapses, we only place tracers in regions above a density threshold, n_{thresh} , related to the Mach number. We set our threshold density for various values of f_{thresh} , defined by

$$n_{thresh} = n_0 \mathcal{M}_0^2 f_{thresh}, \quad (5.1)$$

where n_0 is the initial gas number density and \mathcal{M}_0 is the initial Mach number. This is motivated by the theoretical prediction that a core will be unstable to collapse if its thermal pressure exceeds the mean turbulent pressure (Krumholz & McKee (2005)) giving a critical core density,

$$\rho_c = \langle \rho \rangle \mathcal{M}^2. \quad (5.2)$$

Given that the tracers appear to follow the collapse of the turbulent cloud relatively well even for $n_{tracer} = 1$ and 5 tracers per zone, we can expect good tracking if we

initialize the passive tracers such that $n_{tracer} = n$ in simulations with mean density $n_0 = 100 \text{ cm}^{-3}$.

In order to allow the turbulence to develop and create realistic density structure, we deposit the tracers in the over-dense regions at a time on the order of the turbulent crossing time,

$$\tau = L/v_{turb} = \left(\frac{M_{GMC} L^2}{2E_{kin}} \right)^{1/2} = \left(\frac{5}{6\alpha_{vir} G \rho_0} \right)^{1/2} \quad (5.3)$$

which can be related to the freefall time,

$$t_{ff} = \left(\frac{3\pi}{32G\rho_0} \right)^{1/2} = \left(\frac{9\pi\alpha_{vir}}{80} \right)^{1/2} \tau \quad (5.4)$$

We choose initial conditions that reflect physically realistic turbulent molecular cloud environments. Typical values for the column density of galactic GMCs are $\bar{\Sigma} \sim 170 \text{ M}_\odot \text{ pc}^{-2}$ (Solomon et al. (1987)). Thus we choose our initial density and simulation box size such that $\rho_0 L \sim 0.04 \text{ g cm}^{-2}$. We also set our numerical and physical conditions such that the condition for sink particle creation,

$$\frac{\rho_{LP}(0.5\Delta x)}{\rho_0} = \frac{8.86c_s^2}{\pi G(\Delta x)^2 \rho_0}, \quad (5.5)$$

is sufficiently large, i.e. there is enough contrast between the background density and the star-forming criterion.

5.2 $\alpha_{vir} = 1$, Tracers deposited at $t = 4.9 \text{ Myr}$

We present results for a simulation given initial $\alpha_{vir} = 1$. We initialize our simulation volume with H number density $n_0 = 100 \text{ cm}^{-3}$, corresponding to $2.34 \times 10^{-22} \text{ g cm}^{-3}$. The box size is $L = 20 \text{ pc}$. From Equation 4.6 we have $v_{turb} = 2.67 \text{ km s}^{-1}$ and

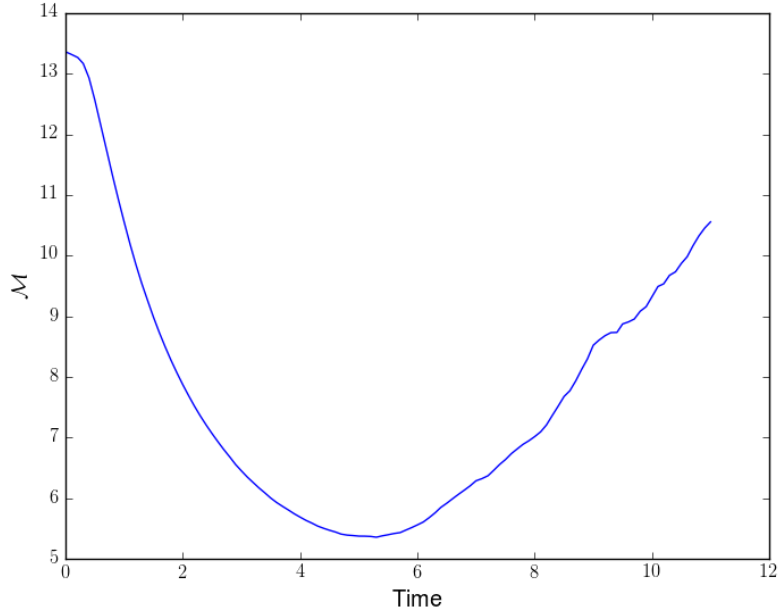


Figure 5.1: The evolution of $\mathcal{M} = \langle v^2 \rangle^{1/2} / c_s$ over the course of the simulation. We see that while the mean velocity initial decreases with time due to decay of turbulent velocities, it increases after $t \sim t_{ff}$ due to the accretion of matter onto sink particles. Time is given in code units, $t_{code} = 0.98$ Myr.

$c_s = 0.2 \text{ km s}^{-1}$, giving us $\mathcal{M}_0 = 13.36$. The values of τ and t_{ff} are 7.4 Myr and 4.4 Myr respectively. With a resolution of 128^3 with 16 processors the simulation had a total runtime of 34 hours.

In Figure 5.1 we show the evolution of the volume averaged \mathcal{M} over the course of the simulation. We see that \mathcal{M} steadily decreases initially, as the turbulent velocity perturbations are applied only at the initial time step and decay with time. However, at $t \sim t_{ff} = 4.4$ Myr we see \mathcal{M} began to steadily increase as material begins to accrete onto the star particles.

We would like to look at the evolution of structure over the course of turbulent collapse, so we want to deposit tracers after dense cores and star particles have formed. Thus, we deposit tracers proportional to the fluid density at $t = 4.9$ Myr, which is of the order of $t_{ff} = 4.4$ Myr and $\tau = 7.4$ Myr. We would also like to determine the origin of the material that accretes onto sink particle regions, so in §5.3 we deposit

tracers at $t = 0.98$ Myr before star particles form. In this simulation, the star particles began to form at $t = 1.6$ Myr. We run the simulation until $t = 10.8$ Myr.

We initialize tracers above a given threshold density so that we can trace the evolution of structure forward in time. At $t = 4.9$ Myr we place tracers in all zones with gas density above $n_{thresh} = 0.05 n_0 \mathcal{M}_0^2 = 892 \text{ cm}^{-3}$. We look at the distribution of a selection of these tracer particles that were initialized at $t = 4.9$ Myr with $n_{init} \geq n_{thresh} = 0.05 f_{thresh} n_0 \mathcal{M}_0^2 = 892 f_{thresh} \text{ cm}^{-3}$, where $f_{thresh} = 1, 10^{0.5}$, and 10. Note that although we are depositing tracers at later times, we scale n_{thresh} with the initial Mach number.

In §5.2.1 we present pseudocolor plots of the column density of the tracers that were initialized above these threshold densities at $t = 4.9$ Myr, and in §5.2.2 we present the final distribution of the tracers at $t = 10.8$ Myr. Tracer column density has been scaled so that it is comparable to the gas density, and star particle positions have been overlaid with color mapped to their mass.

5.2.1 Initial Tracer Distribution

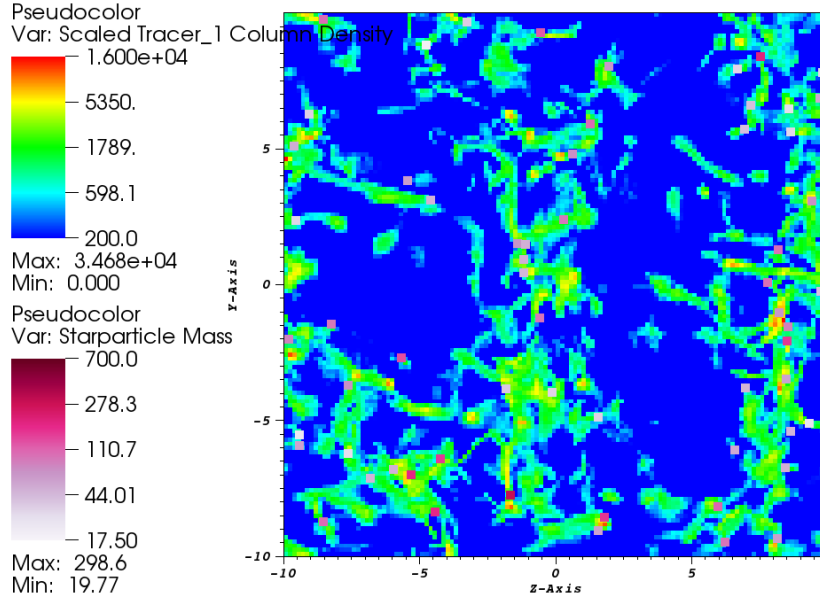
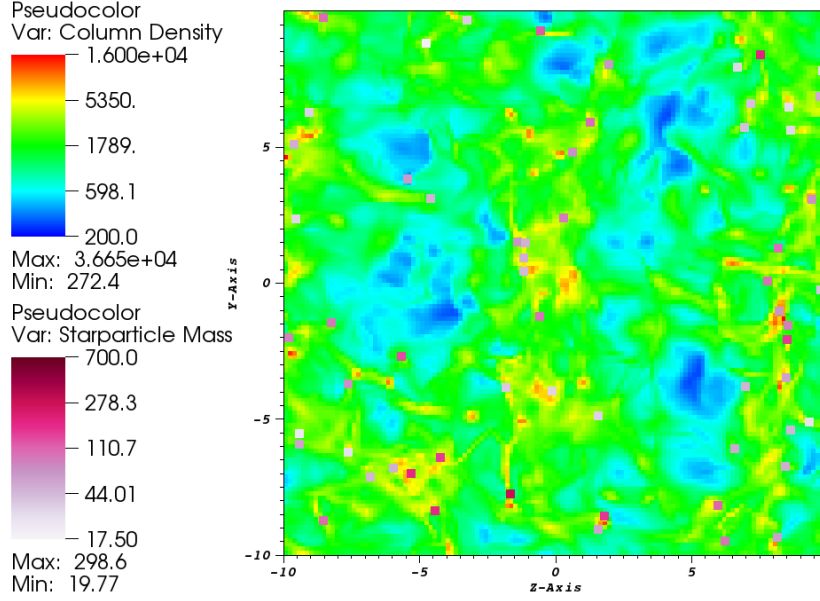


Figure 5.2: Pseudocolor images of the column density ($\text{pc cm}^{-3} = 3.1 \times 10^{18} \text{ cm}^{-2}$) of the fluid (top) and scaled tracer density (bottom) at $t = 4.9 \text{ Myr}$. Tracers initialized above a threshold density, $n_{\text{thresh}} = 0.05 n_0 \mathcal{M}_0^2 = 892 \text{ cm}^{-3}$, are shown. Star particles are overlaid with color mapped to stellar mass (M_\odot).

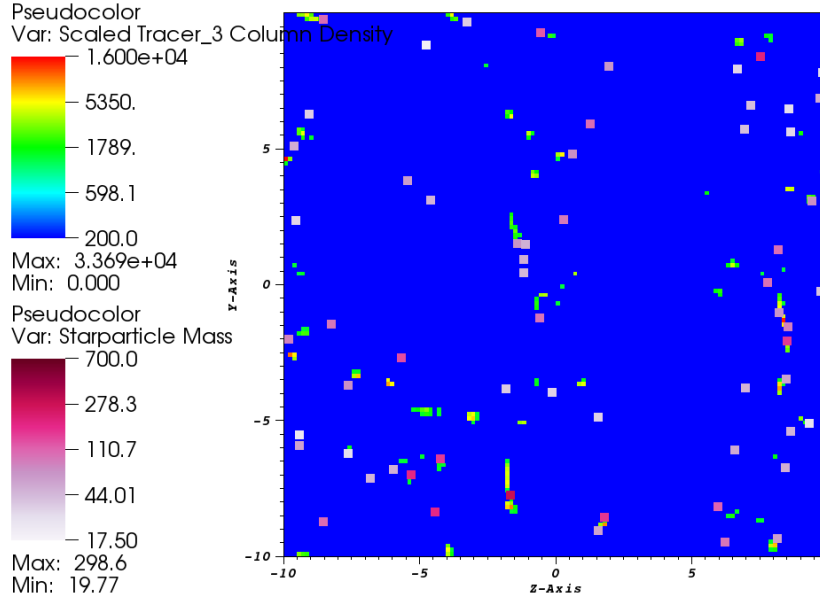
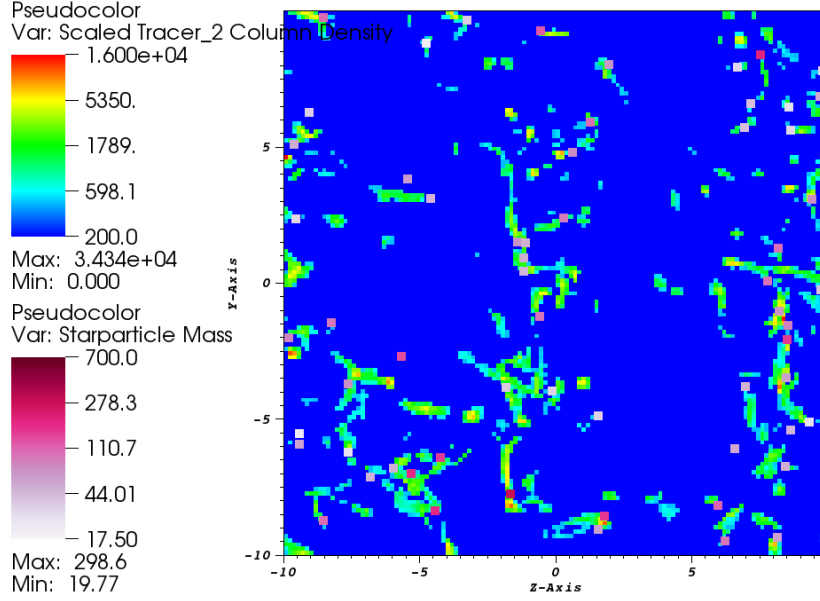


Figure 5.3: Pseudocolor images of the scaled tracer column density ($\text{pc cm}^{-3} = 3.1 \times 10^{18} \text{ cm}^{-2}$) at $t = 4.9 \text{ Myr}$. Tracers initialized above threshold densities $n_{\text{thresh}} = 0.16 n_0 \mathcal{M}_0^2 = 2821 \text{ cm}^{-3}$ (top) and $n_{\text{thresh}} = 0.5 n_0 \mathcal{M}_0^2 = 8920 \text{ cm}^{-3}$ (bottom) are shown. Star particles are overlaid with color mapped to stellar mass (M_\odot).

5.2.2 Final Tracer Distribution

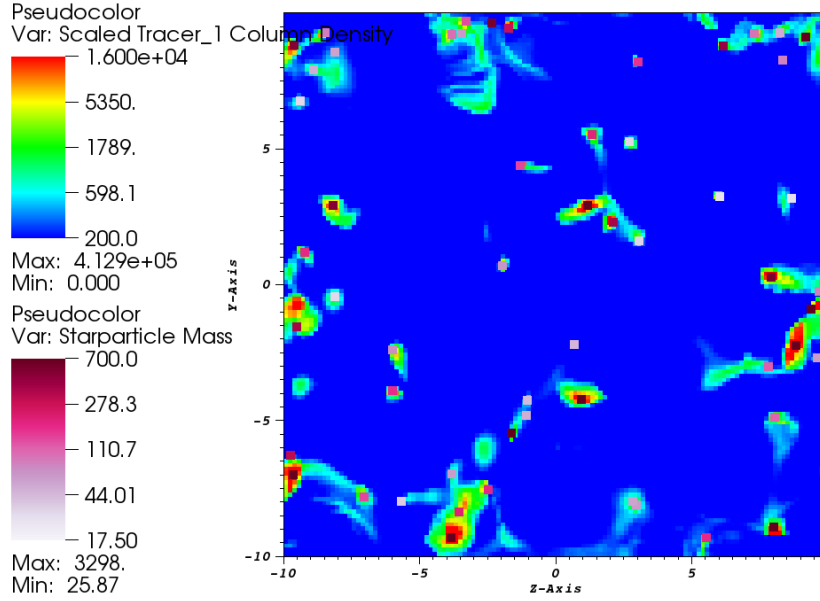
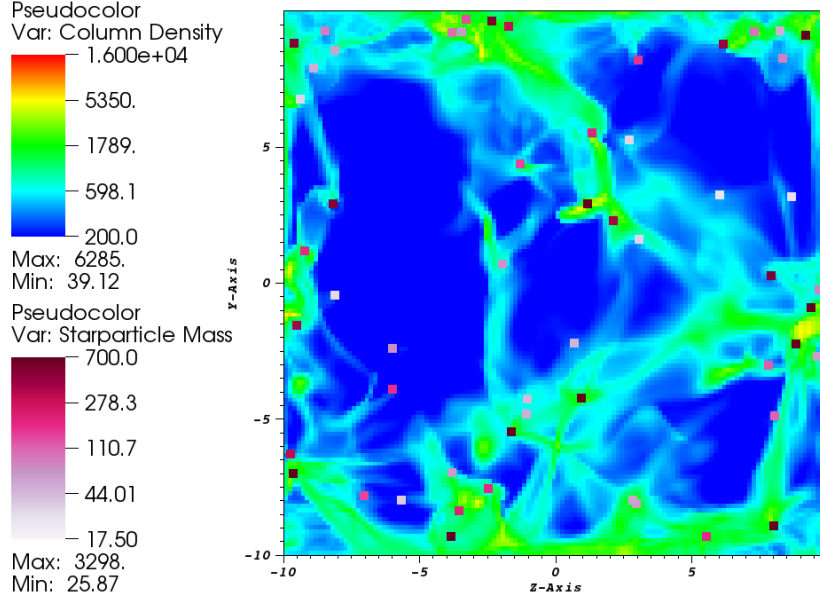


Figure 5.4: Pseudocolor images of the column density ($\text{pc cm}^{-3} = 3.1 \times 10^{18} \text{ cm}^{-2}$) of the fluid (top) and scaled tracer density (bottom) at $t = 10.8$ Myr. Tracers initialized above a threshold density, $n_{\text{thresh}} = 0.05 n_0 \mathcal{M}_0^2 = 892 \text{ cm}^{-3}$, are shown. Star particles are overlaid with color mapped to stellar mass (M_\odot).

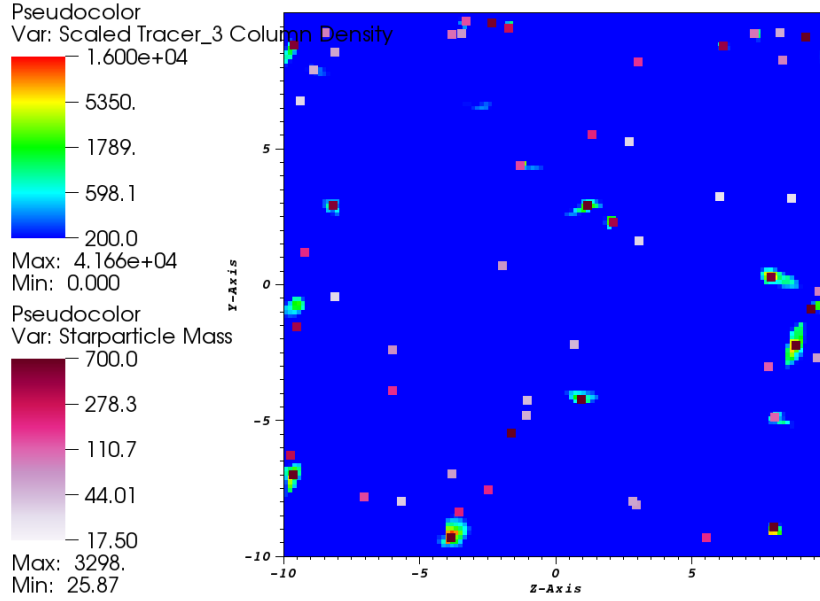
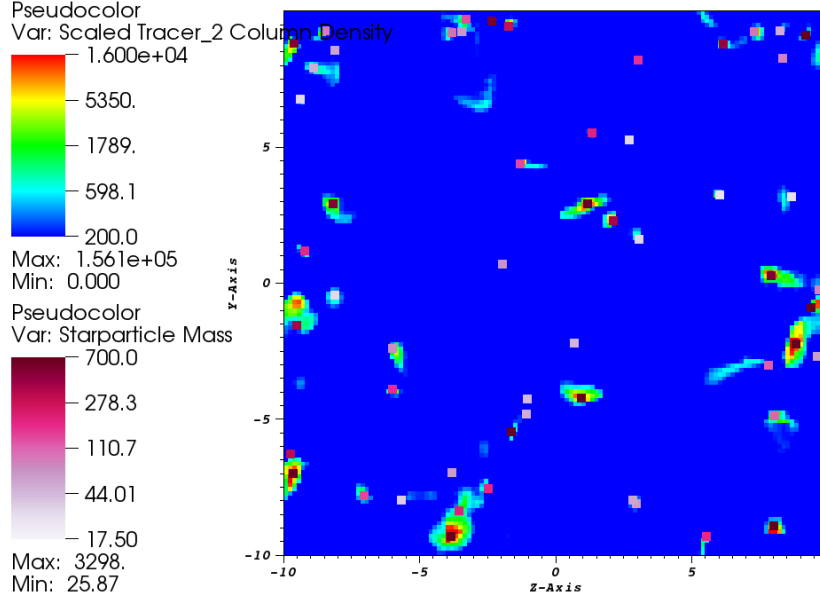


Figure 5.5: Pseudocolor images of the tracer column density ($\text{pc cm}^{-3} = 3.1 \times 10^{18} \text{ cm}^{-2}$) at $t = 10.8 \text{ Myr}$. Tracers initialized above threshold densities $n_{\text{thresh}} = 0.16 n_0 \mathcal{M}_0^2 = 2821 \text{ cm}^{-3}$ (top) and $n_{\text{thresh}} = 0.5 n_0 \mathcal{M}_0^2 = 8920 \text{ cm}^{-3}$ (bottom) are shown. Star particles are overlaid with color mapped to stellar mass (M_\odot).

5.2.3 Discussion and Analysis

In view of §5.2.2, we see that at $t = 10.8$ Myr much of the mass has formed dense filaments and cores. By the end of the simulation the total stellar mass was $22120 M_{\odot}$, or 80% of the total mass. However, with a resolution of 128^3 , only 131 star particles formed with $\langle M \rangle = 168 M_{\odot}$. Thus we can consider the sink particles in these results to be more representative of star clusters than individual stars with this resolution. We see that for the tracers initialized with the lowest density, $n_{thresh} = 0.05 n_0 \mathcal{M}_0^2 = 892 \text{ cm}^{-3}$, many of the tracers do not lie within cores by $t = 10.8$ Myr. At the highest threshold level, $n_{thresh} = 0.5 n_0 \mathcal{M}_0^2 = 8920$, it appears that much of the mass surrounds star particles; however there do remain some regions of low tracer density outside of sink particles.

We can look at these patterns more quantitatively in Figure 5.6. We display the proportion of tracer particles initialized above the three threshold initial densities, n_{thresh} , that have collapsed at any given time. Here we can infer a metric of the fraction of material at various density distributions after the turbulence has developed that eventually ends up accreting onto stars. We note that by $t = 10.8$ Myr at the the highest n_{thresh} almost all the material ends up in stars, $\sim 99\%$, while even at the lowest n_{thresh} a very significant portion of the material ends up in star particles. This is not surprising, as most of the gas accretes onto star particles by the end of the simulation.

If we look at earlier times, $t \sim 7 - 8$ Myr, we see that a much higher proportion of the tracers initialized at lower threshold densities has collapsed. This may indicate that stars may initially accumulate mass preferentially first from higher-density regions before accumulating mass from lower-density regions.

Additionally, we note that the typical time for tracers to collapse into sink particles increases for the tracers initialized at lower density thresholds. This suggests that there may be a relationship between the typical collapse time for a core and its density.

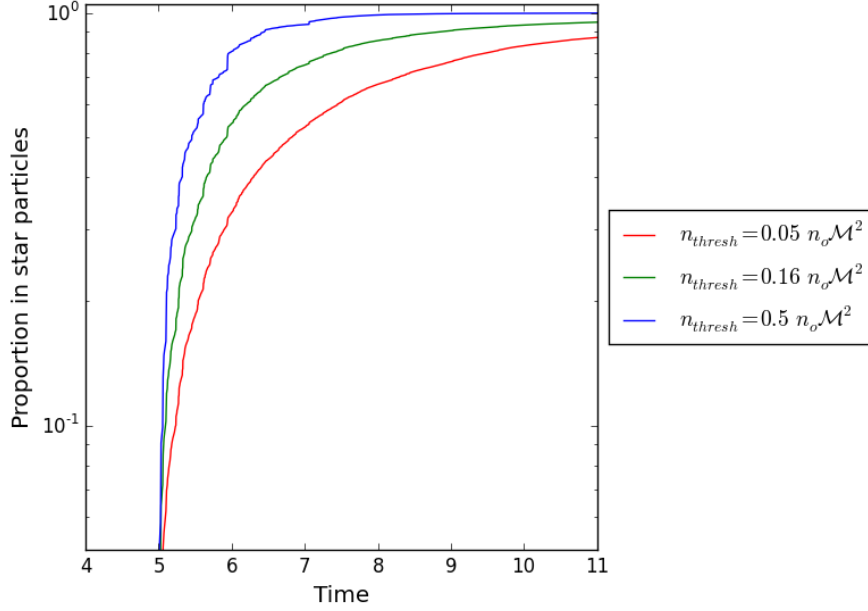


Figure 5.6: The proportion of tracer particles initialized above the three threshold densities, n_{thresh} , that are located in sink particle regions.

Further quantification of the behavior of passive tracers could be used to explore whether the typical time to collapse is related to n_{thresh} , as it has been suggested that the typical collapse time is of the order of the core free-fall time (Vázquez-Semadeni et al. (2005)),

$$t_{fc} = \left(\frac{\pi}{G\rho_c} \right)^{1/2}. \quad (5.6)$$

5.3 $\alpha_{vir} = 1$, Tracers deposited at $t = 0.98$ Myr

In addition to looking at the distribution of initial densities that eventually collapses into sink regions, we would like to look at how over-dense regions evolve forward in time before global collapse sets in and investigate the reservoir of mass that accretes onto star particles. To this end, we initialize a simulation volume with the same initial conditions as in §5.2 but deposit tracers proportional to the fluid density at $t = 0.98$ Myr, before sink particles begin to form at $t = 1.6$ Myr and before $t_{ff} = 4.4$ Myr. We

use the same threshold densities, $n_{thresh} = n_0 \mathcal{M}_0^2 f_{thresh}$ where $f_{thresh} = 0.05, 0.16$, and 0.5 . Again we run the simulation until $t = 10.8$ Myr. With a resolution of 128^3 and running on 16 processors, the simulation had a total runtime of 26 hours. In §5.2.1 we present pseudocolor plots of the column density of the tracers that were initialized above these threshold densities at $t = 0.98$ Myr, and in §5.2.2 we present the final distribution of the tracers at $t = 10.8$ Myr. We scale tracer column density such that it is comparable to the gas column density. Star particles are overlaid for the pseudocolor plots at $t = 10.8$ Myr, with color mapped to stellar mass.

5.3.1 Initial Tracer Distribution

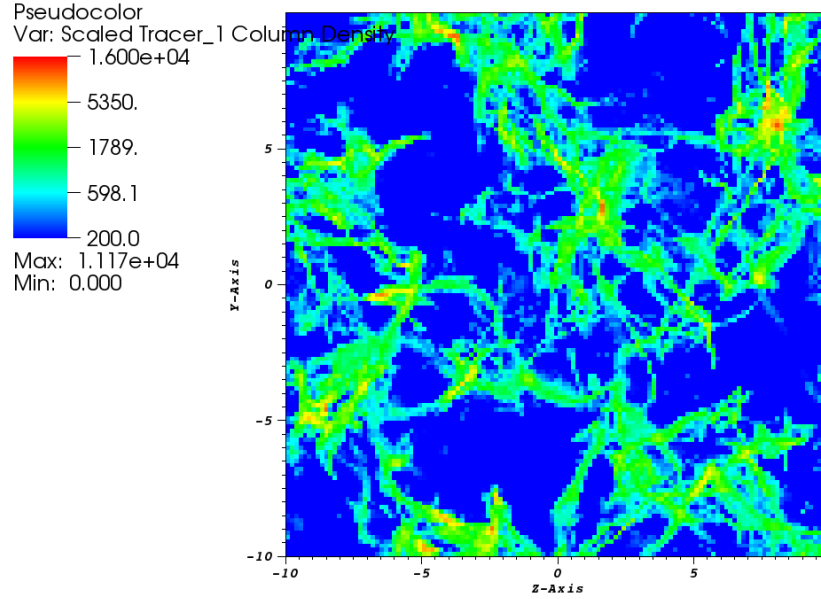
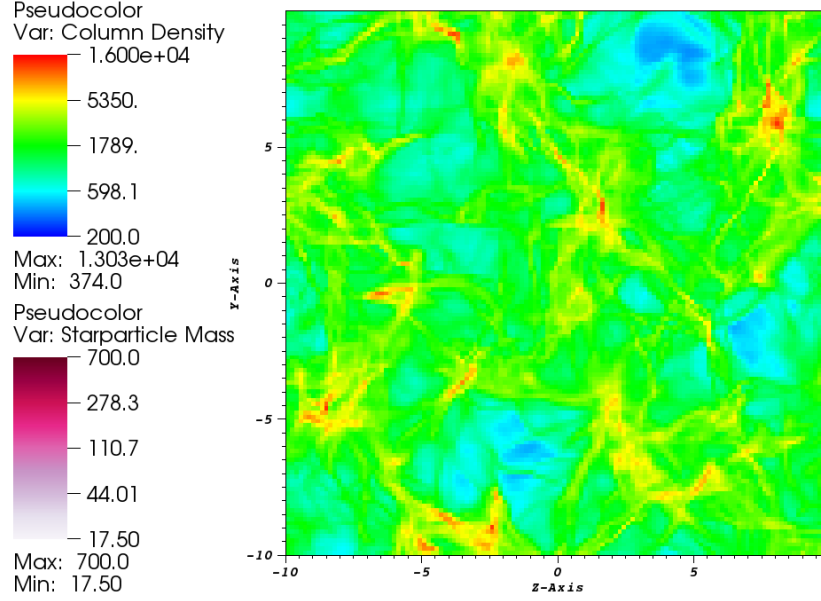


Figure 5.7: Pseudocolor images of the column density ($\text{pc cm}^{-3} = 3.1 \times 10^{18} \text{ cm}^{-2}$) of the fluid (top) and scaled tracer density (bottom) at $t = 0.98 \text{ Myr}$. Tracers initialized above a threshold density, $n_{\text{thresh}} = 0.05 n_0 \mathcal{M}_0^2 = 892 \text{ cm}^{-3}$, are shown. No star particles have formed at this time.

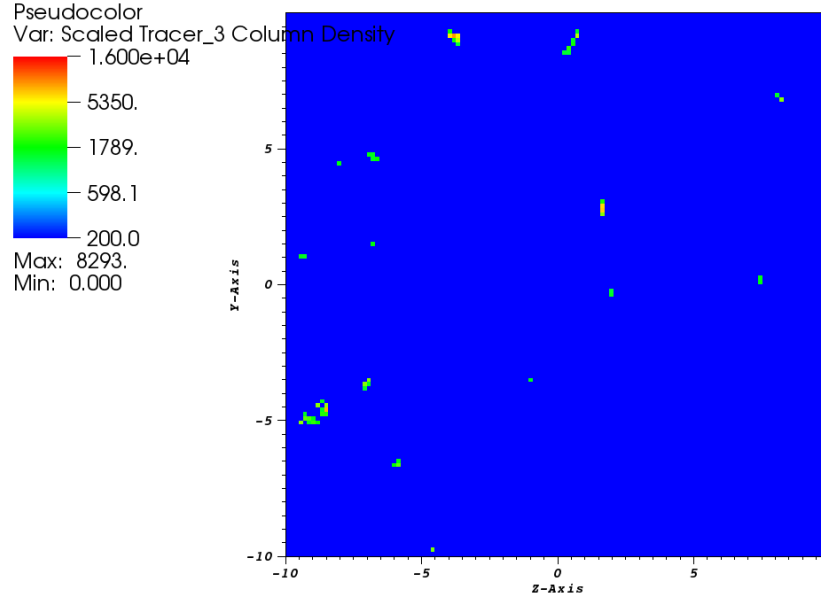
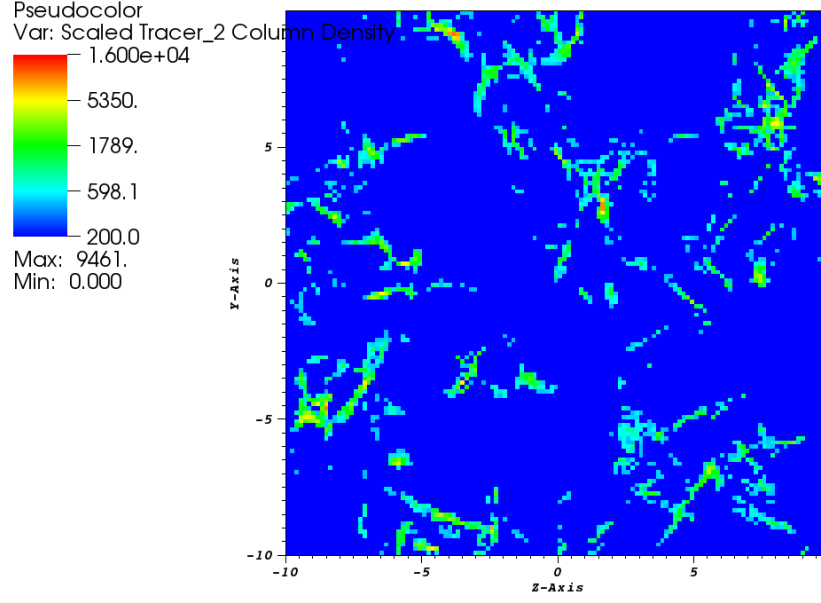


Figure 5.8: Pseudocolor images of the scaled tracer column density ($\text{pc cm}^{-3} = 3.1 \times 10^{18} \text{ cm}^{-2}$) at $t = 0.98 \text{ Myr}$. Tracer initialized above threshold densities $n_{\text{thresh}} = 0.16 n_0 \mathcal{M}_0^2 = 2820 \text{ cm}^{-3}$ (top) and $n_{\text{thresh}} = 0.5 n_0 \mathcal{M}_0^2 = 8920 \text{ cm}^{-3}$ (bottom) are shown. No star particles have formed at this time.

5.3.2 Final Tracer Distribution

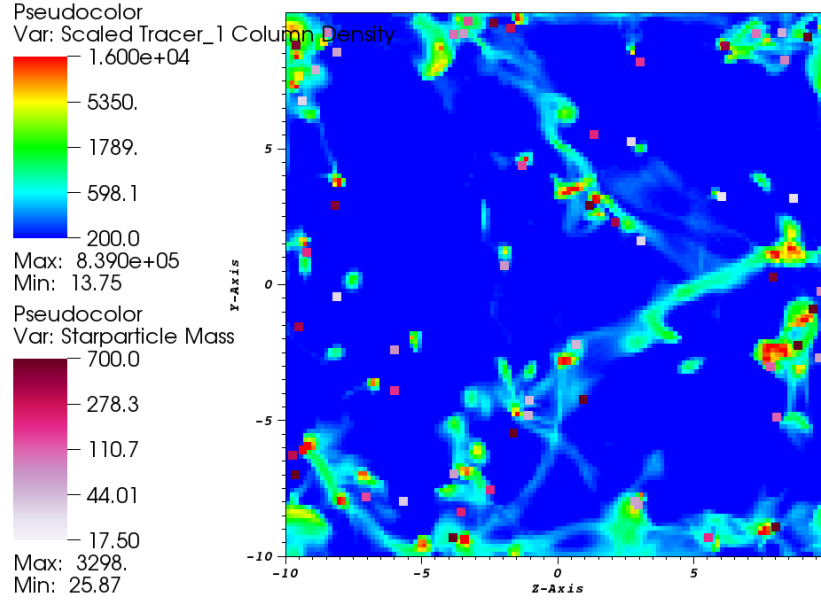
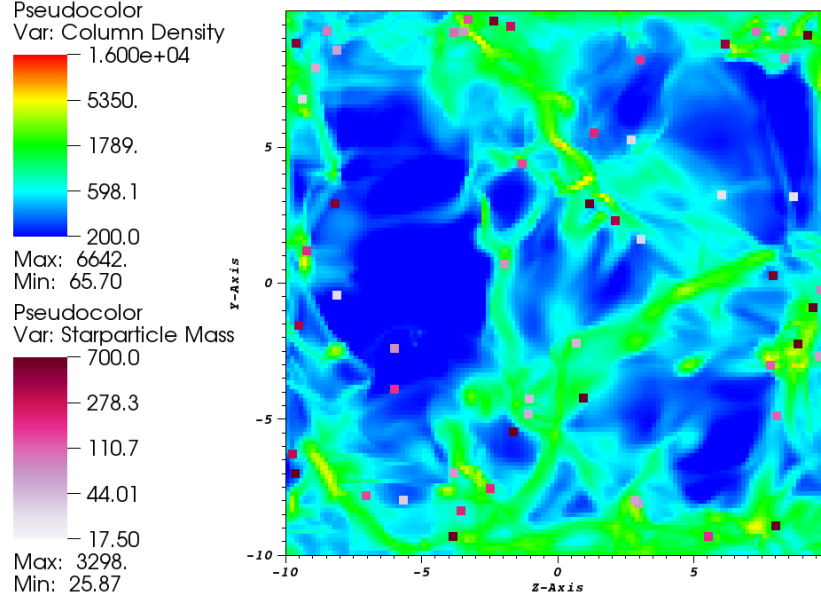


Figure 5.9: Pseudocolor images of the column density ($\text{pc cm}^{-3} = 3.1 \times 10^{18} \text{ cm}^{-2}$) at $t = 10.8 \text{ Myr}$ of the fluid (top) and scaled tracer density (bottom). Tracers initialized above a threshold density, $n_{\text{thresh}} = 0.05 n_0 \mathcal{M}_0^2 = 892 \text{ cm}^{-3}$, are shown. Star particles are overlaid with color mapped to stellar mass (M_\odot).

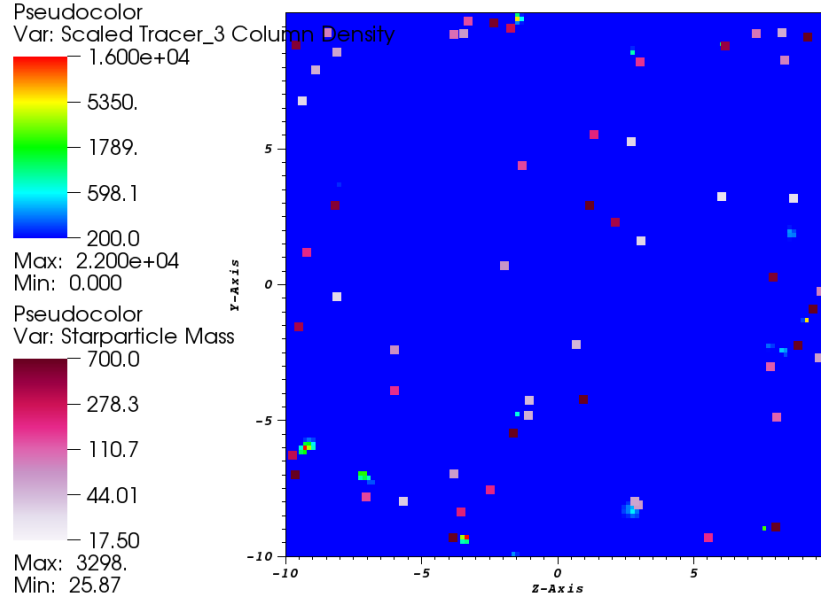
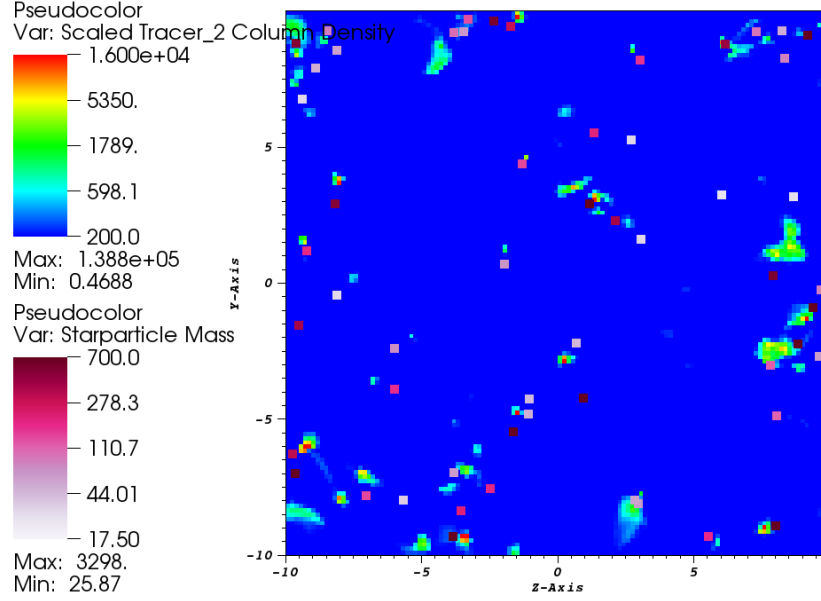


Figure 5.10: Pseudocolor images of the scaled tracer column density ($\text{pc cm}^{-3} = 3.1 \times 10^{18} \text{ cm}^{-2}$) at $t = 10.8 \text{ Myr}$. Tracers initialized above threshold densities $n_{\text{thresh}} = 0.16 n_0 \mathcal{M}_0^2 = 2820 \text{ cm}^{-3}$ (top) and $n_{\text{thresh}} = 0.5 n_0 \mathcal{M}_0^2 = 8920 \text{ cm}^{-3}$ (bottom) are shown. Star particles are overlaid with color mapped to stellar mass (M_\odot).

5.3.3 Analysis and Discussion

In §5.3.1 we see that the turbulent collapse has caused some filamentary structures to form, giving a maximum fluid column density of 13030 pc cm^{-3} . In §5.3.2 we note that while a greater proportion of the tracers initialized at a density threshold of $n_{thresh} = 0.05 n_0 \mathcal{M}_0^2 = 892 \text{ cm}^{-3}$ surround star particle regions, there is still a significant fraction that is present at lower column densities at $t = 10.8 \text{ Myr}$. The tracers initialized with a density threshold of $n_{thresh} = 0.16 n_0 \mathcal{M}_0^2 = 2820 \text{ cm}^{-3}$ visually appear to have a much greater proportion of tracers surrounding star particles with much less equivalent mass in low density regions. At the highest threshold initial density, $n_{thresh} = 0.5 n_0 \mathcal{M}_0^2 = 8920 \text{ cm}^{-3}$, almost all of the tracers appear to be surrounding the sink regions.

We can probe these trends more quantitatively by converting the number of tracers into an equivalent mass and comparing the mass within each initial threshold density to the total stellar mass at a given time. We show the results of this analysis in Figure 5.11. We see that while initially the tracers initialized at $n_{thresh} = 0.05 n_0 \mathcal{M}_0^2$ make up over 90% of the stellar mass, this fraction drops to around 35% by $t = 10.8 \text{ Myr}$. The highest density threshold occupies a very small fraction of the total stellar mass, initially around 30% but dropping to less than 1% by the end of the simulation. These trends support the results seen in § 5.2 and indicate that a great proportion of mass that accretes onto stars is sourced from low-density regions.

In Figure 5.12 we plot the proportion of tracers in star particles for the tracers initialized about the given threshold densities, n_{thresh} , as we did for the tracers initialized at $t = 4.9 \text{ Myr}$. We see that as star particles begin to form from $t = 2 - 4 \text{ Myr}$ the fraction of tracers initialized at each of the threshold densities steadily increases. Comparing with Figure 5.6, we see that the tracers initialized at $t = 4.9 \text{ Myr}$ get incorporated into the sink regions much more rapidly while those initialized at $t = 0.98 \text{ Myr}$ are incorporated more gradually, with the highest threshold density

group, $n_{thresh} = 0.5 n_0 \mathcal{M}_0^2$, having only about 30% of the tracers in sink regions by $t = 4$ Myr. However, at $t = 10.8$ Myr we see that most of the mass in each of the initial threshold groups lies in sink regions. It should be noted that by the end of the simulation 80% of the initial mass lies in the sink regions. We note that about the same fraction of tracers from the $n_{thresh} = 0.05 n_0 \mathcal{M}_0^2$ and $n_{thresh} = 0.16 n_0 \mathcal{M}_0^2$ groups lie in sink regions by the end of the simulation, while about 90% of the tracers from the highest density threshold group, $n_{thresh} = 0.5 n_0 \mathcal{M}_0^2$ lie within sink regions by $t = 10.8$ Myr.

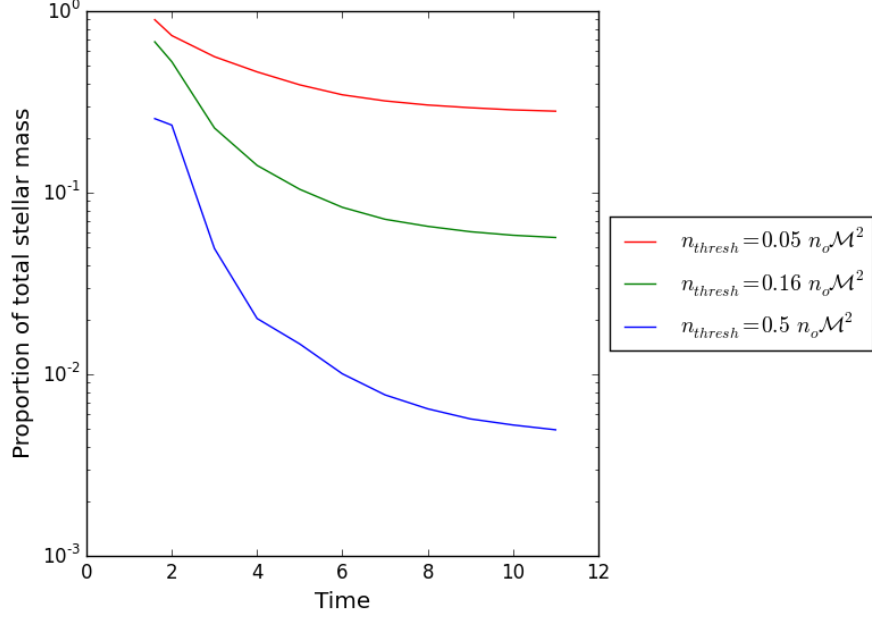


Figure 5.11: The fraction of the total stellar mass that is made up of the equivalent mass in tracer particles initialized above the three threshold densities, n_{thresh} . Time is given in code units, $[t_{code}] = 0.98$ Myr.

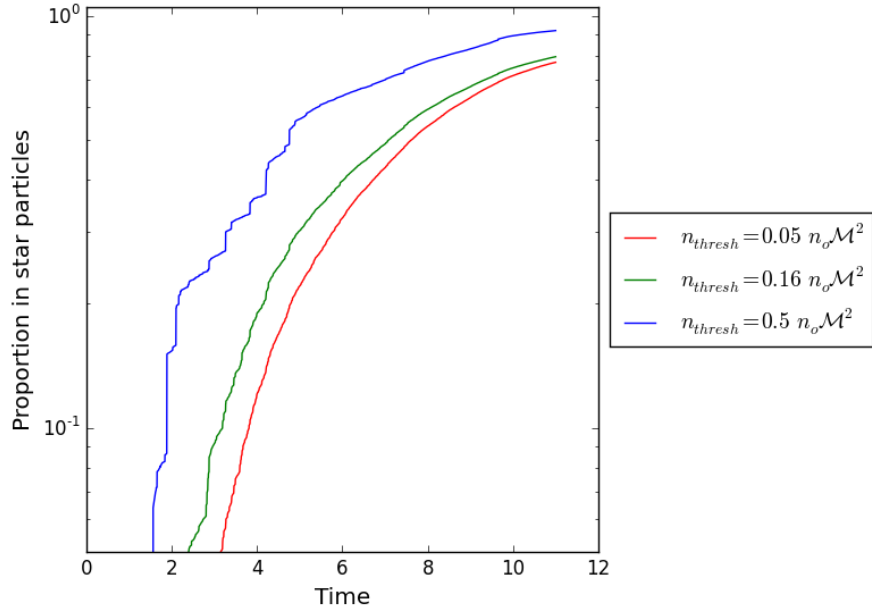


Figure 5.12: The proportion of tracer particles initialized above the three threshold densities, n_{thresh} , that are located in sink particle regions. Time is given in code units, $[t_{code}] = 0.98$ Myr.

5.4 $\alpha_{vir} = 1.5$, Tracers deposited at $t = 4.9$ Myr

We would like to further probe the density threshold relationship for collapse, specifically its dependence on \mathcal{M} . To this end, we initialize a simulation with the same conditions as §5.2 but with $\alpha_{vir} = 1.5$, giving us $\mathcal{M}_0 = 16.4$ and $v_{turb} = 3.2 \text{ km s}^{-1}$.

In Figure 5.13 we show the evolution of \mathcal{M} . We see similar behavior to that shown in Figure 5.1. The turbulent velocity reaches a minimum at $t \sim 5$ Myr, slightly after t_{ff} . We note that \mathcal{M} reaches a minimum value of about 6, slightly higher than that observed for the $\alpha_{vir} = 1$ simulations, as we would expect.

Again we deposit tracers above a density threshold at $t = 4.9$ Myr, which is on the order of $\tau = 5.98$ Myr and $t_{ff} = 3.5$ Myr. From the results in §5.2 we saw that a large proportion of stellar mass is occupied by tracers that originated from the lowest density threshold, $n_{thresh} = 0.05 n_0 \mathcal{M}_0^2$, we choose f_{thresh} such that we can investigate a greater range of density thresholds. In §5.4.1 we present results of the distribution of the fluid density and tracer density as they are deposited at $t = 4.9$ Myr for $f_{thresh} = 10^{-2}, 10^{-1.5}, 10^{-1}$, and 1. in §5.4.1 we present the final distribution for these threshold levels at $t = 10.8$ Myr.

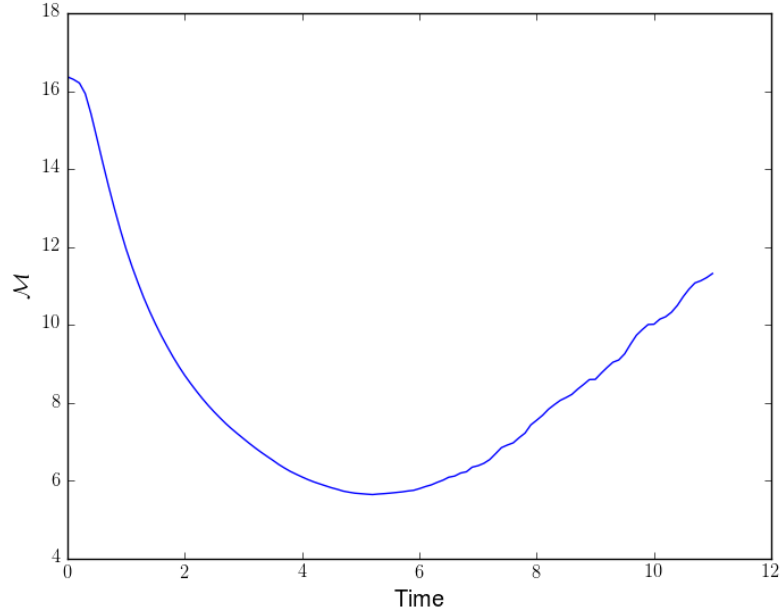


Figure 5.13: The evolution of $\mathcal{M} = \langle v^2 \rangle^{1/2}/c_s$ over the course of the simulation. We see that while the mean velocity initial decreases with time due to decay of turbulent velocities, it increases after $t \sim t_{ff}$ due to the accretion of matter onto sink particles.

5.4.1 Initial Tracer Distribution

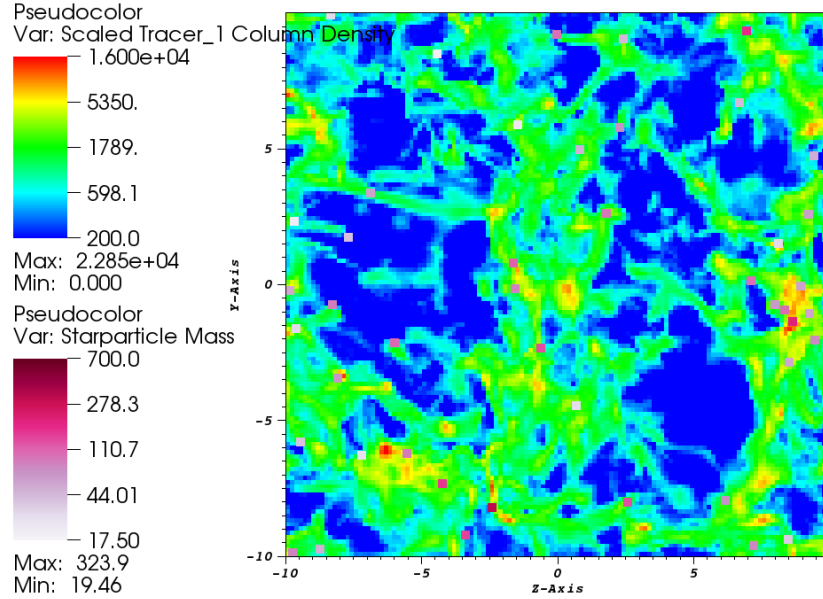
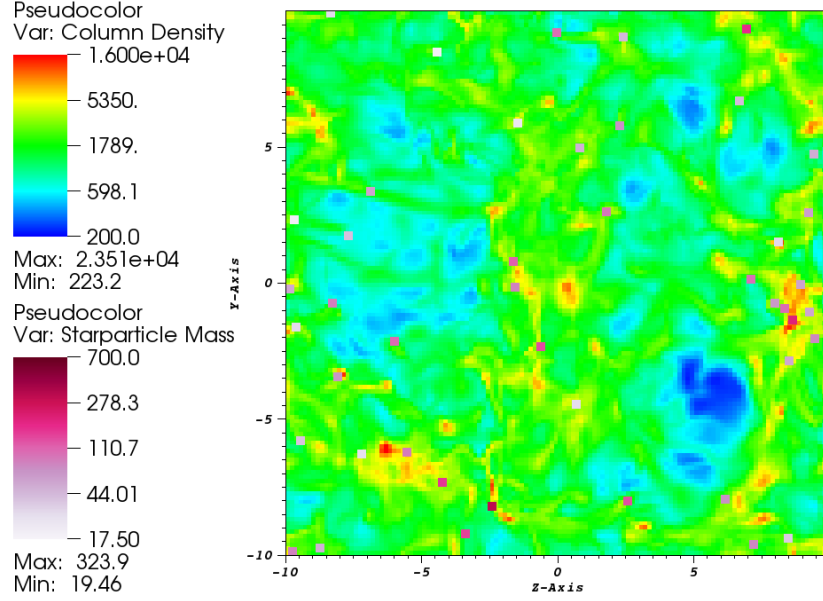


Figure 5.14: Pseudocolor images of the column density ($\text{pc cm}^{-3} = 3.1 \times 10^{18} \text{ cm}^{-2}$) of the fluid (top) and scaled tracer density (bottom) at $t = 4.9$ Myr. Tracers initialized above a threshold density, $n_{\text{thresh}} = 10^{-2} n_0 \mathcal{M}_0^2 = 269 \text{ cm}^{-3}$, are shown. Star particles are overlaid with color mapped to stellar mass (M_\odot).

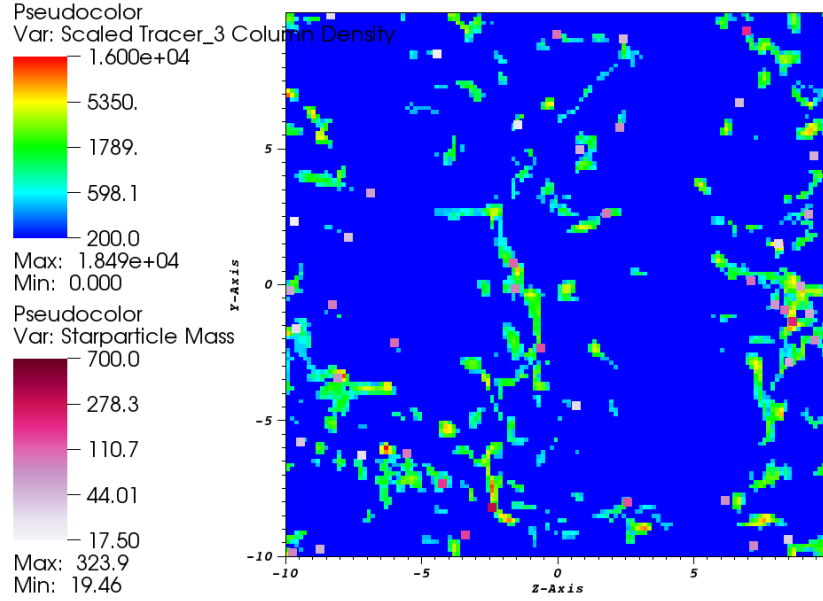
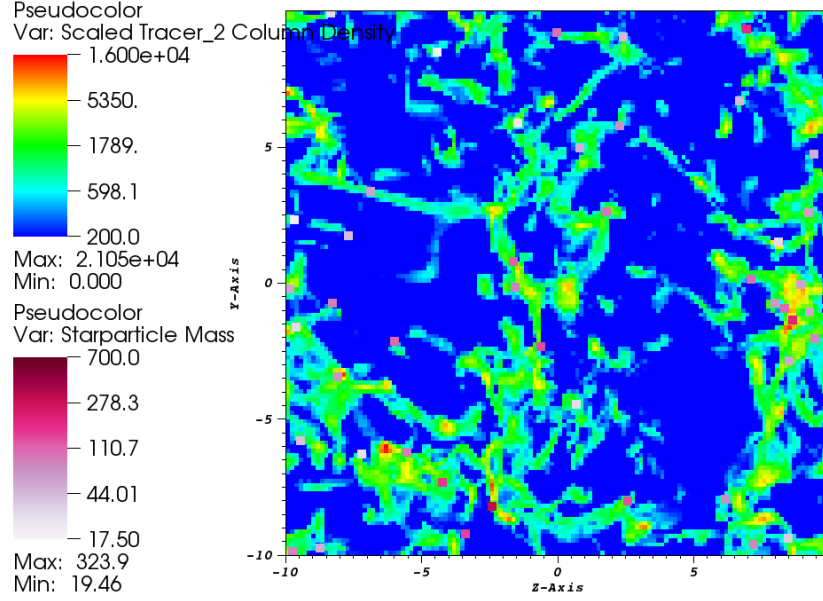


Figure 5.15: Pseudocolor images of the scaled tracer column density ($\text{pc cm}^{-3} = 3.1 \times 10^{18} \text{ cm}^{-2}$) at $t = 4.9 \text{ Myr}$. Tracers initialized above threshold densities $n_{\text{thresh}} = 10^{-1.5} n_0 \mathcal{M}_0^2 = 851 \text{ cm}^{-3}$ (top) and $n_{\text{thresh}} = 10^{-1} n_0 \mathcal{M}_0^2 = 2690 \text{ cm}^{-3}$ (bottom) are shown. Star particles are overlaid with color mapped to stellar mass (M_\odot).

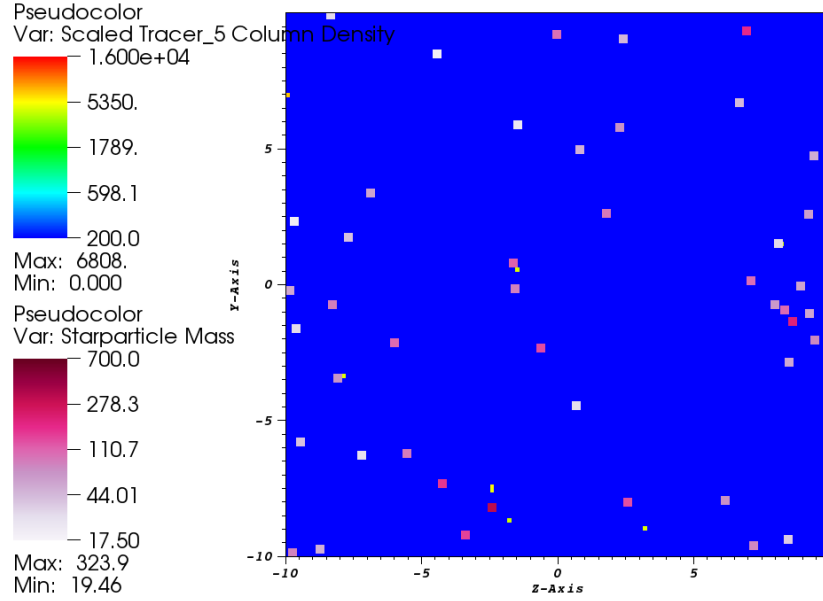
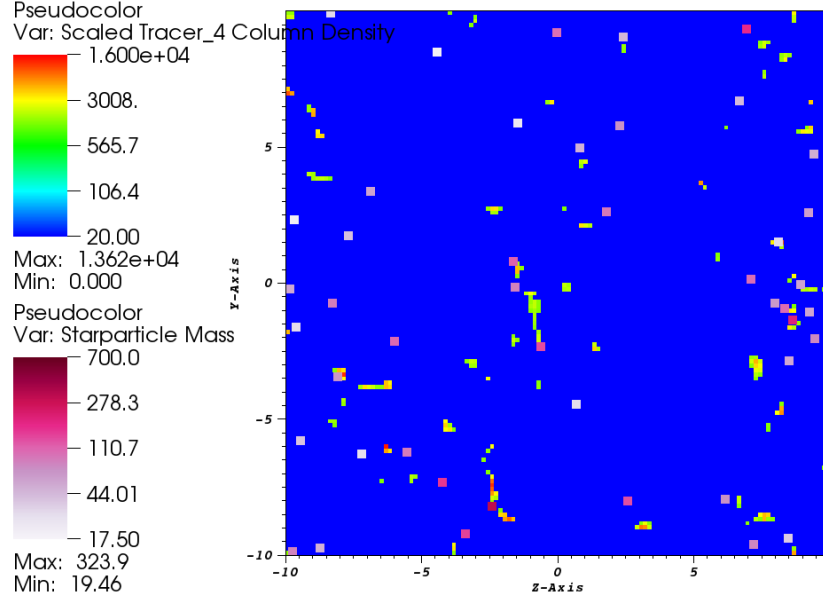


Figure 5.16: Pseudocolor images of the scaled tracer column density ($\text{pc cm}^{-3} = 3.1 \times 10^{18} \text{ cm}^{-2}$) at $t = 4.9 \text{ Myr}$. Tracers initialized above threshold densities $n_{\text{thresh}} = 10^{-0.5} n_0 \mathcal{M}_0^2 = 8505 \text{ cm}^{-3}$ (top) and $n_{\text{thresh}} = n_0 \mathcal{M}_0^2 = 26896 \text{ cm}^{-3}$ (bottom) are shown. Star particles are overlaid with color mapped to stellar mass (M_\odot).

5.4.2 Final Tracer Distribution

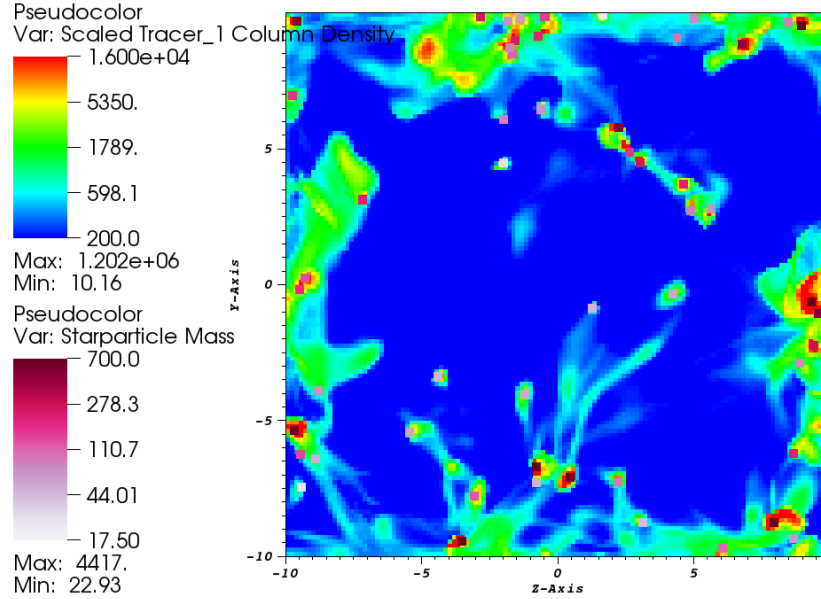
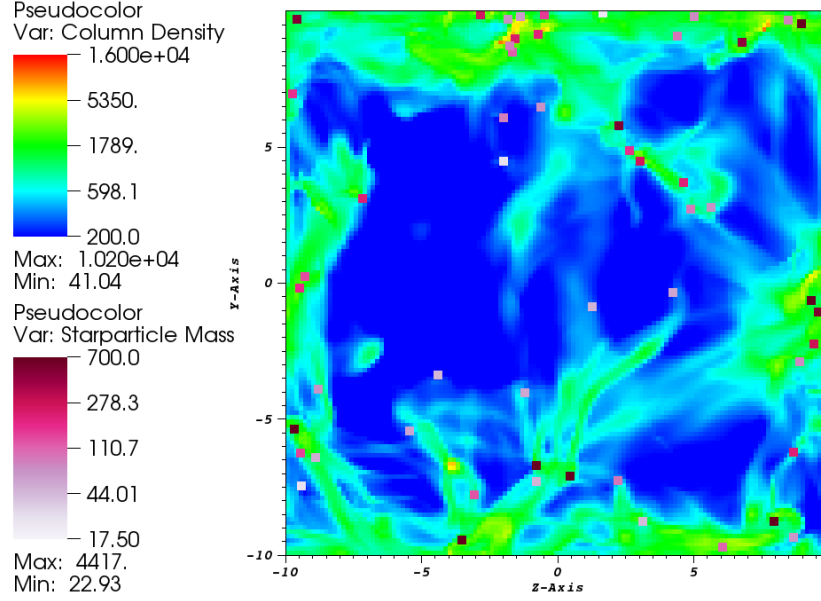


Figure 5.17: Pseudocolor images of the column density ($\text{pc cm}^{-3} = 3.1 \times 10^{18} \text{ cm}^{-2}$) of the fluid (top) and scaled tracer density (bottom) at $t = 10.8$ Myr. Tracers initialized above a threshold density, $n_{\text{thresh}} = 10^{-2} n_0 \mathcal{M}_0^2 = 269 \text{ cm}^{-3}$, are shown. Star particles are overlaid with color mapped to stellar mass (M_\odot).

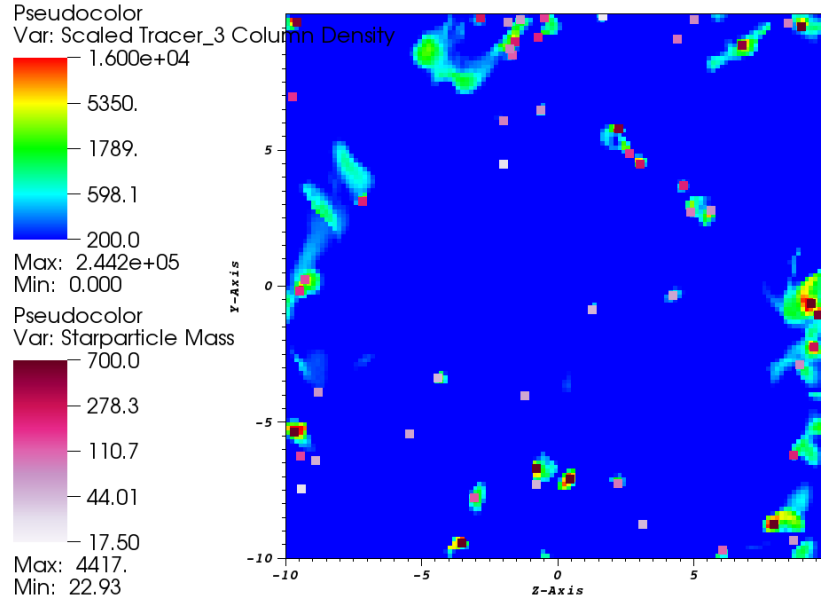
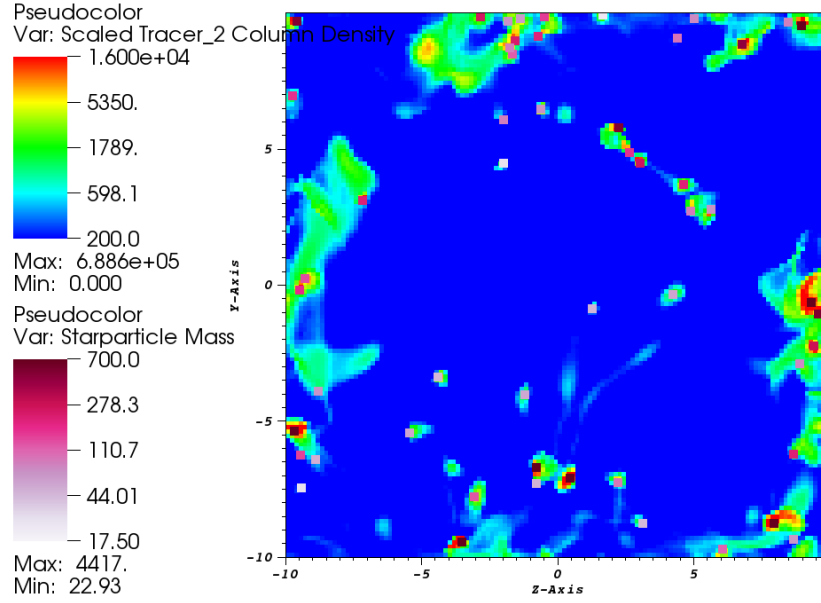


Figure 5.18: Pseudocolor images of the scaled tracer column density ($\text{pc cm}^{-3} = 3.1 \times 10^{18} \text{ cm}^{-2}$) at $t = 10.8 \text{ Myr}$. Tracers initialized above threshold densities $n_{\text{thresh}} = 10^{-1.5} n_0 \mathcal{M}_0^2 = 851 \text{ cm}^{-3}$ (top) and $n_{\text{thresh}} = 10^{-1} n_0 \mathcal{M}^2 = 2690 \text{ cm}^{-3}$ (bottom) are shown. Star particles are overlaid with color mapped to stellar mass (M_\odot).

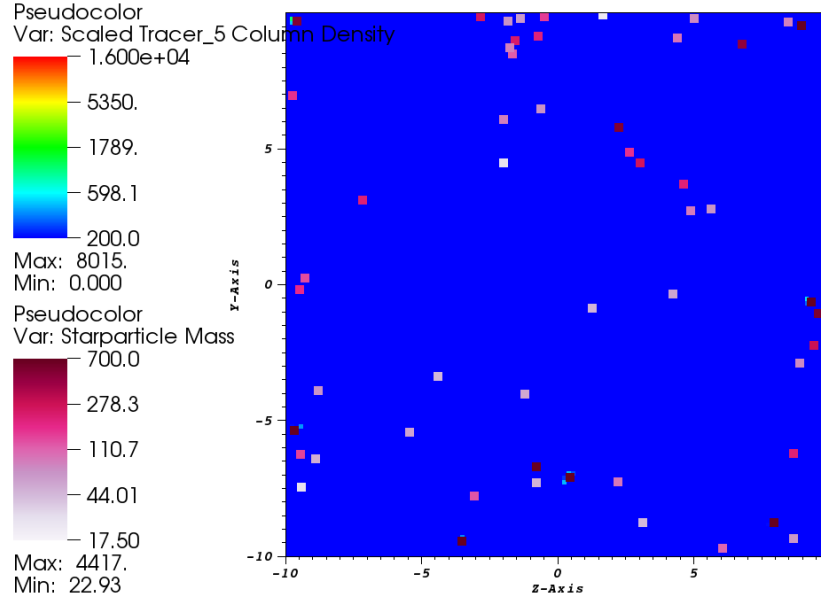
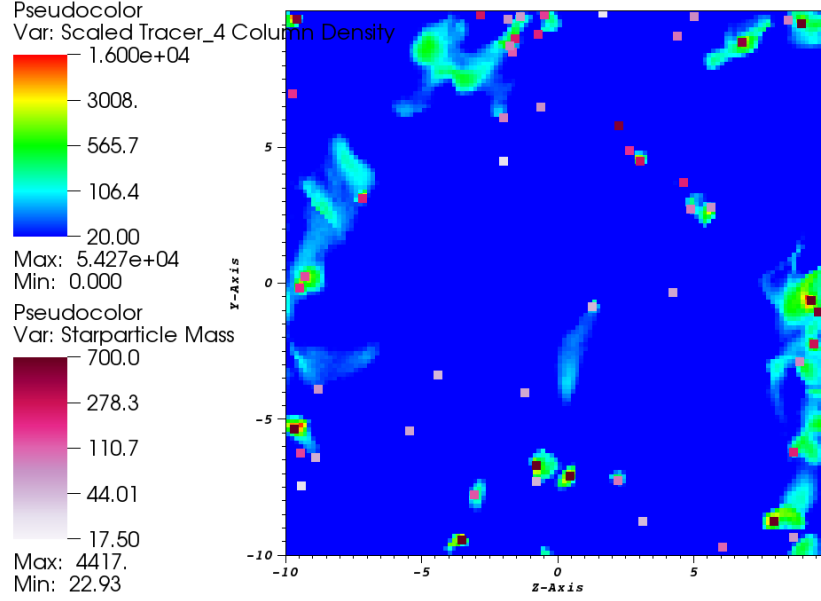


Figure 5.19: Pseudocolor images of the scaled tracer column density ($\text{pc cm}^{-3} = 3.1 \times 10^{18} \text{ cm}^{-2}$) at $t = 10.8 \text{ Myr}$. Tracers initialized above threshold densities $n_{\text{thresh}} = 10^{-0.5} n_0 \mathcal{M}_0^2 = 8505 \text{ cm}^{-3}$ (top) and $n_{\text{thresh}} = n_0 \mathcal{M}_0^2 = 26896 \text{ cm}^{-3}$ (bottom) are shown. Star particles are overlaid with color mapped to stellar mass (M_\odot).

5.4.3 Analysis and Discussion

In §5.4.1 we note that while the structure present in the density field looks very similar to that seen in §5.2.1, the column density has a slightly smaller global maximum of 23510 pc cm^{-3} , as we would expect due to the turbulent support against gravitational collapse. Note that 1.06×10^8 total tracers are deposited at $t = 4.9$, as opposed to 4.9×10^7 tracers in the equivalent $\alpha_{vir} = 1$ simulation, as our lowest density threshold is $n_{thresh} = 10^{-2} n_0 \mathcal{M}_0^2 = 269 \text{ cm}^{-3}$, as opposed to $n_{thresh} = 0.5 n_0 \mathcal{M}_0^2 = 892 \text{ cm}^{-3}$ in the $\alpha_{vir} = 1$ simulation. We see that at time of deposit the tracers initialized at the highest density threshold, $n_{thresh} = n_0 \mathcal{M}_0^2$, appear to all surround the starparticle regions.

In reference to §5.4.2, we see that the tracers initialized at the lowest threshold, $n_{thresh} = 10^{-2} n_0 \mathcal{M}_0^2$, have a large fraction in low-density regions and do not appear to differ very significantly from the fluid column density at $t = 10.8 \text{ Myr}$. However, we do see accumulation of a large number of tracers surrounding the sink regions. If we compare with the results in §5.2.2, we see that for tracers initialized at similar threshold densities ($f_{thresh} = 10^{-1}$ and 0.16 , $10^{-0.5}$ and 0.5), we see that in the $\alpha_{vir} = 1.5$ case there appear to be more tracers occupying the low-density regions as opposed to in the $\alpha_{vir} = 1$ case, where most of the tracers appear to surround sink regions.

Again, we investigate the proportion of the tracers initialized at each of the threshold density that ends up in sink regions at each time step (Figure 5.20). We note that the tracers initialized at the highest density threshold very quickly get incorporated into sink regions. However, only 256676 of the total 1.06×10^8 tracers were initialized at this highest threshold density.

If we compare Figure 5.20 with Figure 5.6, the behavior of the tracers initialized above $n_{thresh} = n_0 \mathcal{M}_0^2$ in the $\alpha_{vir} = 1.5$ case is very similar to the behavior of the tracers initialized above $n_{thresh} = 0.5 n_0 \mathcal{M}_0^2$ in the $\alpha_{vir} = 1$ case. By the end of the simulation, over 90% of the tracers in both groups are occupied in sink regions. If we

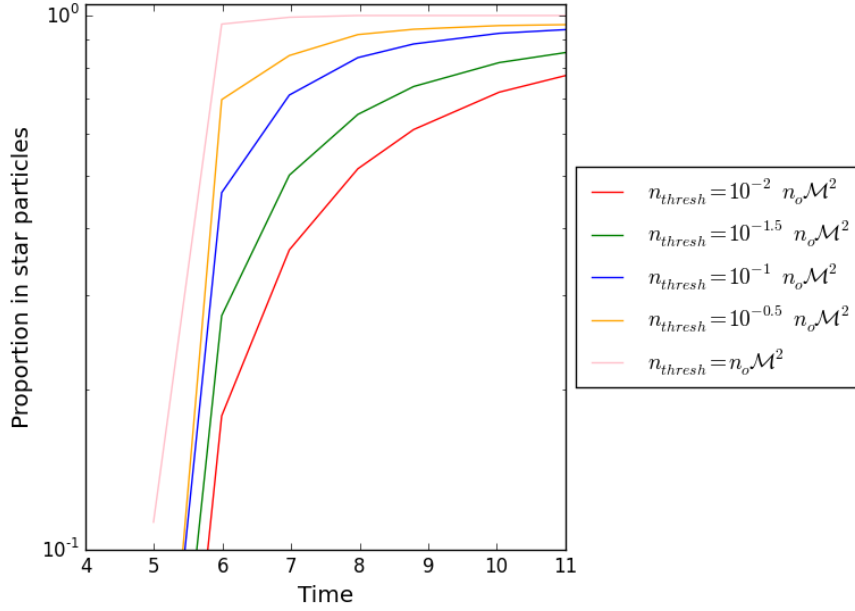


Figure 5.20: The proportion of tracer particles initialized above the three threshold densities, ρ_{thresh} , that are located in sink particle regions. Time is given in code units, $[t_{code}] = 0.98$ Myr.

compare tracers from the $\alpha_{vir} = 1$ and $\alpha_{vir} = 1.5$ simulations of comparable threshold groups ($f_{thresh} = 10^{-1}$ and $0.16, 10^{-0.5}$ and 0.5), we see that for the $\alpha_{vir} = 1.5$ simulation a slightly smaller fraction of tracers end up in sink regions by $t = 10.8$ Myr. Because we note similar behavior with a small increase in \mathcal{M} , we can infer that f_{thresh} , does not depend strongly on \mathcal{M} . Further analysis with higher \mathcal{M} is required to draw any conclusions about the relationship between the timescale and threshold density for collapse of a pre-stellar core and its turbulent environment.

Chapter 6

Conclusions and Future Work

6.1 Summary of Results and Conclusions

In §3 we compared two passive tracer methods, Monte Carlo tracers and velocity field tracers, using several idealized test simulations in ATHENA. We showed that while velocity field tracers, implemented with a second order spatial interpolation, have a lower statistical noise than the Monte Carlo method, the noise of the Monte Carlo method can be minimized by increasing the number of tracers used to track a given mass of fluid. Furthermore, we see that the Monte Carlo method is advantageous because of its relatively low computational cost.

In §4.1 we applied the Monte Carlo passive tracer method to study isothermal supersonic hydrodynamic turbulence. We initialized the tracer number per cell proportional to the fluid density in order to evaluate the tracer method in a turbulent environment. We found that while at low densities the statistical noise of the tracers was much higher than in the idealized case, it is computationally feasible to initialize tracers at much higher densities to track structures within a turbulent molecular cloud.

In §5 we apply the Monte Carlo tracer method to study the turbulent collapse of

GMCs during star formation. We initialize tracers proportional to the fluid density above certain number density thresholds related to the initial Mach number, $n_{thresh} = f_{thresh} n_0 \mathcal{M}_0^2$. To begin, in §5.2 we deposit tracers after the dynamical time, L/v_{turb} , at $t = 4.9$ Myr in order to follow the evolution of structure as the cloud collapses. We find at late time, $t = 10.8$ Myr, that even for the tracers initialized at the lowest density threshold, $n_{thresh} = 0.05 n_0 \mathcal{M}_0^2$, the majority ($\sim 80\%$) of tracers are accreted onto star particles, about the same fraction of total gas mass that had collapsed at that time. The fraction of tracers that end up in sink regions at $t = 10.8$ Myr increases to $\gtrsim 95\%$ as the density threshold is increased to $n_{thresh} = 0.5 n_0 \mathcal{M}_0^2$.

We additionally note that at earlier times, $t \sim 7$ Myr, the relative fraction of tracers initialized at the highest n_{thresh} to lowest n_{thresh} that have collapsed is much greater than at later times. This supports the idea that the typical time for collapse of a pre-stellar core may be related to a threshold density.

In §5.3.2 we deposit tracers before star particles are formed in order to identify the regions that form the mass source for star particles. We see that the majority of the mass that accretes onto star particles at late times, $t \sim 2t_{ff}$, comes from lower density regions, from regions of number density $n \lesssim 0.5 n_0 \mathcal{M}_0^2$. This implies that much of the matter that eventually forms stars may not be sourced from high-density pre-stellar cores but from lower-density surrounding regions. However, at earlier times, $t \sim t_{ff}$, a much larger proportion of the sink particle mass comes from high-initial-density tracers. This suggests that stars may initially form from the highest density gas before accreting from successively lower-density regions.

Finally, in §5.4.2 we present results of a simulation with increased \mathcal{M} by using an initial $\alpha_{vir} = 1.5$. We deposit tracers after global collapse has set in at $t = 4.9$ Myr. We find that the tracers initialized at comparable threshold densities collapsed similarly to those in the $\alpha_{vir} = 1$ simulation. This implies that f_{thresh} is not highly dependent on \mathcal{M} . However, further investigation of the influence of the turbulent

environment on the collapse of dense cores is required.

6.2 Future Work

While we are able to draw some interesting conclusions from these simple models, this work leaves many open research directions for the future. To begin, it is important to ensure that the patterns we see in structure formation are consistent as we increase resolution. In the turbulence simulation we employed a resolution of 128^3 . Since the Larson-Penston criterion for sink region formation, $\rho_{LP} \propto (\Delta x)^{-2}$, at this lower resolution we see the accumulation of large amounts of mass in sink regions, with $\langle M_{star} \rangle \sim 170 M_{\odot}$. Thus the sink regions correspond to the formation of star clusters rather than individual stars. We would like to ensure that as the resolution is increased, we achieve similar behavior for the tracing of structures above given threshold densities.

There are several additional ways we could improve this simple model for the tracing of cores as global collapse occurs. For example, we could initialize tracers dynamically when regions achieve a given threshold density rather than simply following a snapshot of the density distribution at a single point in time. We could also trace the positions of tracers forward in time to construct a correlation function of the mass sources that are eventually accreted onto a single star or stellar system. Due to their comparatively high computational cost we did not apply the velocity field tracers to the turbulence simulation. Perhaps if a small number of these tracers were initialized only in selected structures we could more precisely trace the evolution in spacial and density distribution of the core as collapse occurs.

Bibliography

Agertz, O., Moore, B., Stadel, J., et al. 2007, MNRAS, 380, 963

Bai, X.-N., & Stone, J. M. 2010, ApJS, 190, 297

Bash, F. N., Green, E., & Peters, III, W. L. 1977, ApJ, 217, 464

Blitz, L. 1993, in Protostars and Planets III, ed. E. H. Levy & J. I. Lunine, 125–161

Bonazzola, S., Heyvaerts, J., Falgarone, E., Perault, M., & Puget, J. L. 1987, A&A, 172, 293

Bonnor, W. B. 1956, MNRAS, 116, 351

Brown, E. F., Calder, A. C., Plewa, T., et al. 2005, Nuclear Physics A, 758, 451

Dame, T. M., Hartmann, D., & Thaddeus, P. 2001, ApJ, 547, 792

Dekel, A., & Krumholz, M. R. 2013, MNRAS, 432, 455

Dobbs, C. L., Pringle, J. E., & Burkert, A. 2012, MNRAS, 425, 2157

Dobbs, C. L., Krumholz, M. R., Ballesteros-Paredes, J., et al. 2014, Protostars and Planets VI, 3

Draine, B. 2010, Physics of the Interstellar and Intergalactic Medium, Princeton Series in Astrophysics (Princeton University Press)

Ebert, R. 1955, ZAp, 37, 217

- Elmegreen, B. G. 2000, *ApJ*, 539, 342
- Enßlin, T. A., & Brüggen, M. 2002, *MNRAS*, 331, 1011
- Federrath, C. 2013, *MNRAS*, 436, 1245
- Federrath, C., Glover, S. C. O., Klessen, R. S., & Schmidt, W. 2008, *Physica Scripta* Volume T, 132, 014025
- Frisch, U., & Bec, J. 2001, in *New Trends in Turbulence*, ed. M. Lesieur, A. Yaglom, & F. David, 341
- Genel, S., Vogelsberger, M., Nelson, D., et al. 2013, *MNRAS*, 435, 1426
- Gong, H., & Ostriker, E. C. 2013, *ApJS*, 204, 8
- Hennebelle, P., & Chabrier, G. 2008, *ApJ*, 684, 395
- Heyer, M., Krawczyk, C., Duval, J., & Jackson, J. M. 2009, *ApJ*, 699, 1092
- Jeans, J. H. 1928, *Astronomy and cosmogony*
- Klessen, R. S., Burkert, A., & Bate, M. R. 1998, *ApJLett*, 501, L205
- Kroupa, P. 2001, in *Astronomical Society of the Pacific Conference Series*, Vol. 228, *Dynamics of Star Clusters and the Milky Way*, ed. S. Deiters, B. Fuchs, A. Just, R. Spurzem, & R. Wielen, 187
- Kroupa, P. 2002, *Science*, 295, 82
- Krumholz, M. R., & McKee, C. F. 2005, *ApJ*, 630, 250
- Larson, R. B. 1969, *MNRAS*, 145, 271
- . 1979, *MNRAS*, 186, 479
- . 1981, *MNRAS*, 194, 809

- Larson, R. B., Tinsley, B. M., & Caldwell, C. N. 1980, *ApJ*, 237, 692
- McKee, C. F., & Ostriker, E. C. 2007, *ARA&A*, 45, 565
- Monaghan, J. J. 1992, *ARA&A*, 30, 543
- Nelson, D., Vogelsberger, M., Genel, S., et al. 2013, *MNRAS*, 429, 3353
- Offner, S. S. R., Clark, P. C., Hennebelle, P., et al. 2014, *Protostars and Planets VI*, 53
- Penston, M. V. 1969, *MNRAS*, 145, 457
- Pichon, C., Pogosyan, D., Kimm, T., et al. 2011, *MNRAS*, 418, 2493
- Roman-Duval, J., Federrath, C., Brunt, C., et al. 2011, *ApJ*, 740, 120
- Salpeter, E. E. 1955, *ApJ*, 121, 161
- Sijacki, D., Vogelsberger, M., Kereš, D., Springel, V., & Hernquist, L. 2012, *MNRAS*, 424, 2999
- Solomon, P. M., Rivolo, A. R., Barrett, J., & Yahil, A. 1987, *ApJ*, 319, 730
- Stone, J. M., & Gardiner, T. 2009, *New Astronomy*, 14, 139
- Stone, J. M., Gardiner, T. A., Teuben, P., Hawley, J. F., & Simon, J. B. 2008, *ApJS*, 178, 137
- Stone, J. M., Ostriker, E. C., & Gammie, C. F. 1998, *ApJLett*, 508, L99
- Vázquez-Semadeni, E., Gómez, G. C., Jappsen, A.-K., Ballesteros-Paredes, J., & Klessen, R. S. 2009, *ApJ*, 707, 1023
- Vázquez-Semadeni, E., Kim, J., Shadmehri, M., & Ballesteros-Paredes, J. 2005, *ApJ*, 618, 344

Ward-Thompson, D., & Whitworth, A. 2011, *An Introduction to Star Formation*
(Cambridge University Press)

Williams, J. P., Blitz, L., & McKee, C. F. 2000, *Protostars and Planets IV*, 97

Wong, T., Hughes, A., Ott, J., et al. 2011, *ApJS*, 197, 16